bioRxiv preprint doi: https://doi.org/10.1101/2021.11.13.468347; this version posted November 13, 2021. The copyright holder for this preprint (which was not certified by peer review) is the author/funder. All rights reserved. No reuse allowed without permission.

Three-dimensional structure of the kinetochore-fibers in human mitotic spindles

Robert Kiewisz[1†], Gunar Fabig[1], William Conway[2], Daniel Needleman[2,3,4,5], and Thomas Müller-Reichert[1]

[1]Experimental Center, Faculty of Medicine Carl Gustav Carus, Technische Universität Dresden, 01307 Dresden, Germany

[2]Department of Physics, Harvard University, Cambridge, MA 02138, USA

[3]Department of Molecular and Cellular Biology, Harvard University, Cambridge, MA 02138, USA

[4]John A. Paulson School of Engineering and Applied Sciences, Harvard University, Cambridge, MA 02138, USA

[5]Center for Computational Biology, Flatiron Institute, New York, NY 10010, USA

†Current address of R. Kiewisz: Simons Machine Learning Center, New York Structural Biology Center, New York, NY 10027, USA

Correspondence to:

T. Müller-Reichert

E-mail: mueller-reichert@tu-dresden.de

Phone: +49 351 458 6442

bioRxiv preprint doi: https://doi.org/10.1101/2021.11.13.468347; this version posted November 13, 2021. The copyright holder for this preprint (which was not certified by peer review) is the author/funder. All rights reserved. No reuse allowed without permission.

Abstract

During cell division, kinetochore microtubules (KMTs) provide a physical linkage between the spindle poles and the chromosomes. KMTs in mammalian cells are organized into bundles, so-called kinetochore-fibers (k-fibers), but the ultrastructure of these fibers is currently not well characterized. Here we show by large-scale electron tomography that each k-fiber in HeLa cells in metaphase is composed of approximately nine KMTs, only half of which reach the spindle pole. Our comprehensive reconstructions allowed us to analyze the three-dimensional (3D) morphology of k-fibers in detail, and we find that they exhibit remarkable variation. K-fibers display differences in circumference and KMT density along their length, with the pole-facing side showing a splayed-out appearance. We further observed that the association of KMTs with non-KMTs predominantly occurs in the spindle pole regions. Our 3D reconstructions have implications for models of KMT behavior and k-fiber self-organization as covered in a parallel publication applying complementary live-cell imaging in combination with biophysical modeling (Conway et al., 2021). The presented data will also serve as a resource for further studies on mitosis in human cells.

bioRxiv preprint doi: https://doi.org/10.1101/2021.11.13.468347; this version posted November 13, 2021. The copyright holder for this preprint (which was not certified by peer review) is the author/funder. All rights reserved. No reuse allowed without permission.

Introduction

Chromosome segregation during cell division is carried out by microtubule (MT)-based spindles (Anjur-Dietrich et al., 2021; McIntosh et al., 2013; Oriola et al., 2018; Prosser and Pelletier, 2017). While mitotic spindles can contain thousands of MTs, only a fraction of those highly dynamic filaments is associated with the kinetochores. These MTs are called kinetochore microtubules (KMTs) and function to establish a physical connection between the chromosomes and the spindle poles (Flemming, 1879; Khodjakov et al., 1997; Maiato et al., 2004; Musacchio and Desai, 2017; Rieder, 1981; Rieder and Salmon, 1998).

Mitotic KMTs show various patterns of organization in different species. Single KMTs are connected to the kinetochores, in budding yeast (Winey et al., 1995), while multiple KMTs are connected to dispersed kinetochores in nematodes (Fabig et al., 2020; Redemann et al., 2017). Multiple KMTs are also connected to kinetochores in human cells. KMTs in human cells are organized in bundles, termed “kinetochore (k)-fibers”, which are attached to a single spot on each chromosome (Begley et al., 2021; Godek et al., 2015; Inoué, 1953; Metzner, 1894; Mitchison and Kirschner, 1984; O’Toole et al., 2020; Schmidt, 1939).

The regulation of KMT dynamics in mitotic spindles has been studied in great detail in a number of different systems, including the early *Caenorhabditis elegans* embryo, *Xenopus* egg extracts and mammalian tissue culture cells (DeLuca et al., 2006; Dumont and Mitchison, 2009; Farhadifar et al., 2020; Inoué and Salmon, 1995; Kuhn and Dumont, 2019; Long et al., 2020). Our understanding of the ultrastructure of KMTs in mammalian k-fibers, however, is rather limited due to a low number of three-dimensional (3D) studies on spindle organization. Earlier studies applied several techniques. Some studies used serial thin-section transmission electron microscopy (TEM) (McDonald et al., 1992; McEwen et al., 1998, 1997) and partial 3D reconstruction by electron tomography. Other studies used serial block-face imaging by scanning electron microscopy to analyze the ultrastructure of mitotic spindles (Hoffman et al., 2020; Nixon et al., 2017, 2015). However, these prior studies did not present comprehensive 3D reconstructions of mammalian mitotic spindles. Nevertheless, by applying serial thin-section TEM it was reported that k-fibers in PtK_1 cells are composed of about 20 KMTs (McDonald et al., 1992; McEwen et al., 1997). In contrast, tomographic analysis of RPE-1 cells revealed 12.6 ± 1.7 KMTs per k-fiber (O’Toole et al., 2020). This variation in the reported numbers of KMTs per k-fiber as well as a lack of complete 3D models of human mitotic spindles motivated us to perform an in-depth analysis of the k-fiber organization and KMT length distribution in the context of whole mitotic spindles in human tissue culture cells.

bioRxiv preprint doi: https://doi.org/10.1101/2021.11.13.468347; this version posted November 13, 2021. The copyright holder for this preprint (which was not certified by peer review) is the author/funder. All rights reserved. No reuse allowed without permission.

Two opposing models of k-fiber organization can be drawn. First, a direct connection between kinetochores and spindle poles can be considered (**Fig. 1A**), in which all KMTs in a given k-fiber have approximately the same length and are rigidly connected (Rieder, 1981; Ris and Witt, 1981). As for the length of the KMTs, previous electron microscopic analyses of chemically fixed PtK_1 and RPE-1 cells have shown short KMTs associated with kinetochores (McDonald et al., 1992; Sikirzhytski et al., 2018). This suggested that not all KMTs in the k-fiber are of the same length, implying that not all KMTs are associated with the spindle poles. Second, an indirect connection may be considered (**Fig. 1B**). In such a model, none of the KMT minus ends would be directly associated with the spindle poles, thus KMTs would show differences in their length and connect to the poles purely by interactions with non-KMTs in the spindle (Sikirzhytski et al., 2018, 2014). However, the kinetochore-to-spindle pole connection in human cells may be neither direct nor indirect, thus showing a semi-direct pattern of connection, in which only some of the KMTs of each k-fiber is associated with the spindle pole while others are not. Previously, we have shown such a semi-direct pattern of KMT anchoring into the spindle network for the first embryonic mitosis in the nematode *Caenorhabditis elegans* (Redemann et al., 2017). Some KMTs in this system are indeed directly associated with the spindle poles, while others are not.

Here we aimed to determine the number and the length of KMTs, and the positioning of their putative minus ends in human k-fibers. Focusing on metaphase, we applied serial-section electron tomography to produce large-scale reconstructions of entire mitotic spindles of HeLa cells and developed software tools for a quantitative in-depth analysis of both KMTs and non-KMTs. We found that k-fibers in HeLa cells are composed of approximately nine KMTs of variable length. These k-fibers display a previously unexpected variable morphology: they did not resemble an organized and compacted structure throughout their whole length. For better visualization of spindle and k-fiber morphology, we introduce a new 3D visualization tool that allows the interested reader to interactively display the 3D data (https://cfci.shinyapps.io/ASGA_3DViewer/).

bioRxiv preprint doi: https://doi.org/10.1101/2021.11.13.468347; this version posted November 13, 2021. The copyright holder for this preprint (which was not certified by peer review) is the author/funder. All rights reserved. No reuse allowed without permission.

Results

K-fibers are composed of approximately nine KMTs

For our large-scale analysis of mammalian k-fibers, we acquired data on metaphase spindles in HeLa cells by serial-section electron tomography (**Fig. 2A-B**). In three full reconstructions, we segmented the spindle poles (including the centrioles), the chromosomes and all MTs (**Fig. 2C-E**). These metaphase spindles were composed of approximately 6300 MTs (6278 ± 1614 MTs, mean ± STD; **Table 1**) and had an average pole-to-pole length of 9.0 ± 1.7 µm (mean ± STD; **Figure 2-figure supplement 1A-B)**.

We then annotated the KMTs in our reconstructions based on the association of the putative MT plus ends with kinetochores. KMTs that were arranged in parallel and made end-on contact at a single 'spot' on the chromosomes were designed as being part of the same k-fiber (**Figure 1-movie supplement 1-3**). In our three data sets, we identified between 90 and 110 k-fibers per cell, which included on average 859 ± 218 KMTs (mean ± STD; n = 3; **Fig. 2F-H**; **Figure 1-movie supplement 4-6**) in each spindle. Thus, only ~14% of all MTs in the reconstructed spindles were KMTs, which corresponds to ~24% of tubulin mass (Conway et al., 2021). The identified KMTs displayed open flared ends at the kinetochore (**Fig. 2-figure supplement 2**), consistent with previous observations of the morphology of KMT plus ends (McIntosh et al., 2013; O'Toole et al., 2003). We took advantage of these extracted k-fibers to further analyze the distance between the sister kinetochores in each data set by measuring the median position of the KMT plus ends (**Figure 2-figure supplement 1C-D**). The average distance between sister kinetochores was 1.1 ± 0.2 µm.

Next, we extracted individual k-fibers from our full 3D reconstructions to visualize their overall morphology (**Fig. 3A** and **Figure 3-movie supplements 1-6**). The individual k-fibers showed remarkable differences in their overall shapes. Some k-fibers were rather straight, while others were very curved. In addition, k-fibers showed variability in their compactness as defined by the density of KMTs in a given k-fiber). At the site of KMT attachment to the chromosomes, k-fibers showed a compacted appearance, while k-fibers were considerably splayed out at the site facing the spindle poles. Moreover, some pole proximal KMT ends extend beyond the position of the spindle poles.

We next investigated the number of KMTs per kinetochore (**Fig. 3B** and **Figure 3-figure supplement 1A**) and found that the k-fibers were composed of 8.5 ± 2.2 KMTs (mean ± STD, n = 293). Previously published data indicated that the number of KMTs is correlated with kinetochore size (McEwen et al., 1998) so that larger kinetochores are associated with more

bioRxiv preprint doi: https://doi.org/10.1101/2021.11.13.468347; this version posted November 13, 2021. The copyright holder for this preprint (which was not certified by peer review) is the author/funder. All rights reserved. No reuse allowed without permission.

KMTs. Therefore, we estimated the size of the kinetochores in our three reconstructed spindles by determining the cross-sectional area of the k-fibers close to the kinetochores. The average kinetochore area was 0.07 ± 0.05 μm^2 (mean ± STD; **Figure 3-figure supplement 1C-D**; while the Poisson correlation coefficient between the number of KMTs and kinetochore area was 1.96 with $p = 1.91 \times 10^{-8}$). This is in line with an observation on the kinetochore area in HeLa cells as analyzed by light microscopy (Cherry et al., 1989). Moreover, we also observed a packing density of KMTs at the kinetochore of 0.07 ± 0.05 KMTs/μm^2 (mean ± STD, n = 293; **Figure 3-figure supplement 1E**; **Table 3**) with average center-to-center distance between KMTs of 64 ± 19 nm (mean ± STD, n = 293; **Figure 3-figure supplement 1F**; **Table 3**). Considering a MT diameter of 25 nm in our data sets, this corresponds to an average 40 nm wall-to-wall spacing between the KMTs at the kinetochore. With this observation we concluded that KMTs tend to be highly compacted at the kinetochore and that kinetochore size does not influence KMT packaging density or the distance between KMTs. We also investigated a possible influence of the inter-kinetochore distance on the number of MTs attached to the kinetochores. We plotted both the number of attached KMTs and the difference in the number of KMTs attached to sister kinetochores against the inter-kinetochore distance. We did not observe a correlation between these parameters (**Fig 3C-D**; Pearson's correlation coefficients were 0.04 and 0.29) and concluded that the inter-kinetochore distance does not play a significant role in determining the number of KMTs in metaphase.

We next sought to characterize the kinetochore-to-spindle pole connection in more detail. Therefore, we developed software to analyze the structure of KMTs in individual k-fibers (Kiewisz and Müller-Reichert, 2021). We investigated the distribution of KMT lengths and the positioning of KMT minus ends along the spindle axis (**Fig. 4A**). We were specifically interested in the percentage of KMT minus ends that were directly associated with the spindle poles. Similar to a previously published analysis in *C. elegans* (Redemann et al., 2017), we defined a cutoff distance for an MT-centrosome interaction. We used a cutoff distance of 1.53 µm which was twice the half-width of the peak of non-KMT ends near the pole (**Fig. 4B**, grey area). Thus, we considered KMT minus ends within 1.53 µm from the center of the mother centriole to be directly attached to the pole and KMT minus ends positioned further than the 1.53 µm cutoff to be indirectly attached to the pole.

We then continued by measuring the length of all KMTs in our reconstructions (**Fig. 4C; Figure 4-figure supplement 1A**) and observed a broad distribution of KMT lengths with an average value of 3.7 ± 1.8 µm (mean ± STD; n = 2489). This analysis suggested the existence of relatively short KMTs in k-fibers not associated with the spindle poles. Indeed, about 21 ± 4% of the KMTs had lengths less than 2 µm. Our analysis also revealed relatively long KMTs (about 35 ± 10%) that were longer than the half spindle length. Some of these long KMTs

bioRxiv preprint doi: https://doi.org/10.1101/2021.11.13.468347; this version posted November 13, 2021. The copyright holder for this preprint (which was not certified by peer review) is the author/funder. All rights reserved. No reuse allowed without permission.

showed a pronounced curvature at their pole-facing side, thus connecting to the 'back side' of the spindle poles (see also **Fig. 3A**, spindle #II). We then analyzed the distances of the KMT minus ends to the spindle poles (**Fig. 4D**; **Figure 4-figure supplement 1B**). Taking our determined cutoff value into account, we found that only about 50% (54.4 ± 9.3%; mean ± STD, n = 3) of the KMTs were associated with the spindle poles, while the other half of the KMTs were not (**Figure 3-figure supplement 1B**). This suggests that half of the KMTs are indirectly connected to the spindle poles.

We also observed that the number of KMT minus ends associated with the spindle pole was significantly greater in fibers positioned in the center compared to those at the periphery of the mitotic spindle (**Figure 4-figure supplement 2**). We next investigated the relative position of the KMT minus ends on the pole-to-kinetochore axis (**Fig. 4E**; **Figure 4-figure supplement 1C**). We found that KMT minus ends that were positioned within the centrosomal association zone showed a peak position close to the spindle pole center. In contrast, KMT minus ends not associated with a spindle pole did not show a preferred position but rather displayed a flat relative distribution on the pole-to-kinetochore axis. This analysis confirmed our initial visual 3D inspection of the KMTs, revealing that the k-fibers in HeLa cells are not composed of compact bundles of KMTs of the same length but rather of KMTs of different lengths. Importantly, our data analysis also showed that only half of the KMTs in k-fibers are directly associated with the spindle poles.

For comparison, we also analyzed the length distribution of non-KMTs in the spindles. Non-KMTs had an average length of 2.0 ± 1.6 µm (mean ± STD; n = 9957; **Fig. 4F**; **Figure 4-figure supplement 1D**), with many very short MTs and fewer long MTs. In addition, 39 ± 9% of the non-KMT minus ends were localized in the MT-centrosome association zone (**Fig. 4G**; **Figure 4-figure supplement 1E**) with the remaining ~60% in the bulk of the spindle (**Fig. 4H**; **Figure 4-figure supplement 1F**).

K-fibers show a splayed-out appearance at spindle poles

The variable morphology of k-fibers within spindles motivated us to further analyze the 3D structure of individual KMTs in the k-fibers. For this, we measured the tortuosity of individual KMTs. Tortuosity is the ratio of the total length of a curve (the spline length of a given KMT) to the distance between its ends (given here by the 3D Euclidean distance between the KMT ends). Straight KMTs will have a tortuosity of 1 while a quarter circle has tortuosity of around ~1.1 and a half-circle around ~1.6 (**Fig. 5A**). We aimed to measure both the global and the local tortuosity of the KMTs in our reconstructions, i.e., the tortuosity of the KMTs along their entire length and also in defined sections of 500 nm length along the k-fibers, respectively

bioRxiv preprint doi: https://doi.org/10.1101/2021.11.13.468347; this version posted November 13, 2021. The copyright holder for this preprint (which was not certified by peer review) is the author/funder. All rights reserved. No reuse allowed without permission.

(**Fig. 5B-C**). Firstly, we visualized the global tortuosity of individual KMTs by applying a color code. We detected differences in the curvature of individual KMTs (**Fig. 5D**, and **Figure 5-movie supplement 1-3**). For all data sets, we observed an average value of KMT tortuosity of 1.09 ± 0.09 (mean ± STD, n = 2489; **Fig. 5F**) with 32 ± 10% of KMTs showing a tortuosity higher than 1.1. We could also observe that straight KMTs were predominantly located in the center of the spindle with an average tortuosity of 1.07, while more curved KMTs were located more at peripheral spindle positions with an average tortuosity of 1.09 (**Fig. 5E**; **Figure 5-figure supplement 1**). This indicates that the majority of KMTs in the spindle are rather straight and do not show a curvature that is close to a quarter of a circle. Furthermore, the tortuosity of KMTs was correlated with their length (R = 0.65; p = 2.2e-16; **Fig. 5G**) with short MTs being more straight and longer MTs more curved. In addition, 68 ± 13% of the KMTs with a tortuosity higher than 1.1 were longer than the half-spindle length. Secondly, we also investigated the local tortuosity of the KMTs. (**Fig. 5H**). Our analysis revealed that the local tortuosity of the KMTs was correlated with the relative position of the KMT segments on the pole-to-kinetochore axis. In general, the tortuosity of KMTs was not uniform along their entire length but increased at positions closer to the spindle poles. (R = -0.30; p = 2.2e-16; **Fig. 5I**).

Next, we asked whether an increase in k-fiber tortuosity at the pole-facing end is reflected in the overall KMT organization, i.e., in a change in the compactness of the k-fibers along their entire length. For this, we analyzed the cross-section area of the k-fibers by determining their polygon areas (**Fig. 6A**, and **Figure 6-figure supplement 1**) and plotting these areas against the relative position on the pole-to-kinetochore axis (**Fig. 6B**). K-fibers had an average cross-section area of 0.07 ± 0.11 μm^2 (± STD, n = 293). Compared to the kinetochore-facing side of the k-fibers, the polygon area was 10-fold higher at the mid-position of the k-fiber and 5-fold lower at the pole-facing end of the fibers. Moreover, at the pole-facing side, the k-fiber area showed a higher spread of the values, reflecting the splayed-out appearance of the k-fiber at the spindle poles. To further characterize the arrangement of the KMTs in the k-fibers, we also set out to measure the density of the KMTs along the length of the k-fibers (**Fig. 6C**). For each k-fiber, we defined a minimum circle enclosing all KMTs at the kinetochore side. We then measured the number of KMTs that were enclosed in the selected radius at positions along the k-fibers and plotted the percentage of the enclosed KMTs against the relative position along the pole-to-kinetochore axis. We observed a variation in the percentage of enclosed KMTs along the k-fiber length with the highest percentage at the kinetochore and a lower percentage in the pole-facing side of the reconstructed k-fibers (**Fig. 6D**). From all these analyses we concluded that k-fibers display a high tortuosity and a low density of KMTs close to the spindle poles, thus leading to an overall splayed-out appearance of the fibers at their pole-facing end.

bioRxiv preprint doi: https://doi.org/10.1101/2021.11.13.468347; this version posted November 13, 2021. The copyright holder for this preprint (which was not certified by peer review) is the author/funder. All rights reserved. No reuse allowed without permission.

KMTs primarily associate with non-KMTs at spindle poles

We next investigated the pattern of association of KMTs with the neighboring non-KMTs. We were particularly interested in mapping KMT/non-KMT associations along the spindle axis. To describe this association, we considered two types of interactions between MTs. Firstly, we analyzed potential interactions between MT ends with neighboring MT lattices, which could be mediated by MT minus-end associated molecular motors, such as dynein (Tan et al., 2018) or kinesin-14 (Molodtsov et al., 2016), or by γ-tubulin (Rosselló et al., 2018). Secondly, we considered MT-MT lattice interactions, which might be established by molecular motors such as kinesin-5 (Falnikar et al., 2011). We started our analysis by investigating possible KMT minus-end associations with either non-KMT or KMT lattices. For this, we annotated all KMT minus ends in our 3D reconstructions and measured the distance of each minus end to a neighboring MT lattice (**Fig. 7A**). We then determined what percentage of all KMT minus ends were associated with non-KMT lattices according to selected association distances. We considered different possible association distances between KMT minus ends and the neighboring MT lattices (i.e., 25, 30, 35, 45, 50, 75 and 100 nm; **Fig. 7B**; **Table 4** and **Table 5**). As expected, we observed that the number of KMT minus ends associated with adjacent MT lattices increased with an increase in the distance of association. Considering 35 nm as an example for a possible interaction distance between two MTs connected by a single dynein motor (Amos, 1989), we observed that only 41.4 ± 6.3% of the KMT minus ends were associated with other MTs (for a visualization of the pattern of association see **Fig. 7C**; **Figure 7-movie supplement 1**). Moreover, of the KMT minus ends that were not associated with the spindle poles (i.e., the ones positioned farther than 1.53 µm away from the centrioles) only 40.9 ± 5.4% showed an association with other MT lattices at a given distance of 35 nm (**Fig. 7D-E**). This suggested that for this given distance of association roughly only 40% of the KMT minus ends in k-fibers were associated with the MT network. Further considering larger distances of association between KMT minus end and neighboring MTs (**Fig. 7B** and **Fig. 7D**), we also observed that not all KMT minus ends were associated with neighboring MTs even at a value of 100 nm (**Table 4** and **Table 5**).

Next, we sought to map the detected associations of KMT minus ends with either KMT or non-KMT lattices within the reconstructed spindles. For this, we determined the position of such associations in half spindles and plotted the data against the relative spindle position (i.e., against the normalized spindle pole-to-kinetochore distance). We first plotted the number of KMT minus end associations with KMT lattices against the relative position on the spindle axis (**Fig. 7F**). As a result, associations of KMT minus ends with KMT lattices were distributed along the whole half spindle length with a preference for positions at the spindle poles. As an

bioRxiv preprint doi: https://doi.org/10.1101/2021.11.13.468347; this version posted November 13, 2021. The copyright holder for this preprint (which was not certified by peer review) is the author/funder. All rights reserved. No reuse allowed without permission.

example, for a given association distance of 35 nm, 47.5 ± 13.8% of the total number of associations were observed at the spindle poles. We then also determined the relative position of the KMT minus end associations with non-KMT lattices (**Fig. 7G**). Similarly, the majority of the associations of KMT minus ends with non-KMT lattices were observed at the spindle pole. Similarly, at a chosen distance of 35 nm, 51.1 ± 14.7% of these associations were observed at the spindle poles. Thus, the spindle pole appeared as a 'hotspot' for the interaction of KMT minus ends with neighboring MT lattices.

Vice versa, we also determined the occurrence of either KMT minus or non-KMT pole-proximal ends in the vicinity of KMT lattices (**Figure 7-figure supplement 1**; **Table 6** and **Table 7**). For this analysis, we assumed that the end of each non-KMT that is closer to the centrioles represents the minus end. At a distance of 35 nm or closer to the KMT lattice, we observed that on average 43 ± 8 % of KMTs associated with either KMT or non-KMT minus ends, with the majority of associations with non-KMT minus ends (73 ± 4%). Moreover, we also determined the relative position of these associations on the spindle axis. Again, the majority of KMT lattices (59.8 ± 6.7%) associated with other MT minus ends were preferentially found at spindle poles. In contrast, only 39.1 ± 4.6% of non-KMTs associated with other MT minus ends were found at the poles. Again, this analysis indicated that the interaction of KMTs with other MTs preferentially takes place at the spindle poles regardless of the association distance (**Figure 7-figure supplement 1**).

Next, we also considered the length of these MT-MT associations in the spindles. For such a length analysis, we identified individual associations of a minimal length of 20 nm and determined their position and number along the spindle axis (**Fig. 8A**). The minimal length of 20 nm was selected as a fixed distance step size to minimize computational efforts and unify all analyses. In addition, we also varied the distance between associated MTs by choosing values of 25, 30, 35, 45 and 50 nm. Firstly, we analyzed the association of KMTs with other MTs in the spindle by plotting the number of associations (i.e., the number of the 20 nm intervals) against the relative position on the normalized spindle axis. For all considered distances between MTs, we observed peaks of associations at positions close to the spindle poles and a drastic decline in the number of associations at positions in the middle of the spindle (**Fig. 8B-C**; **Figure 8-movie supplement 1**). Secondly, we also analyzed the association of non-KMTs with other MTs. In contrast to the previous analysis, we found that these interactions were spread over the entire length of the spindle without any 'hotspots' of associations for small distances between 25 and 35 nm between MTs (**Fig. 8D-E**; **Figure 8-movie supplement 2**). In fact, similar distribution patterns could be observed for all chosen association distances. This indicated to us that the observed MT-MT association patterns for

bioRxiv preprint doi: https://doi.org/10.1101/2021.11.13.468347; this version posted November 13, 2021. The copyright holder for this preprint (which was not certified by peer review) is the author/funder. All rights reserved. No reuse allowed without permission.

both KMTs and non-KMTs were not dependent on the chosen association distances. We also concluded from these findings that KMTs and non-KMTs differ in their spatial pattern of MT-MT association, with KMTs strongly coupling with neighboring MT at the spindle poles, and non-KMTs showing a more even distribution of MT-MT associations along the spindle axis.

We were also interested in how the distribution pattern of MT-MT interaction changes in relation to the position in the spindle. With our high-resolution 3D datasets covering all MTs in the spindle, we decided to investigate the number and the length of associations for both KMTs and non-KMTs as a function of the distance between MTs. Firstly, we plotted the number of KMTs against the number of associations and also against the length of associations (**Figure 8-supplement 1**). In general, with an increase in the distance between MTs, KMTs showed an increase in the number and also in the average length of interactions (**Table 8** and **Table 9**). For a given MT-MT distance of 35 nm, the number of associations was 14 ± 6 (±STD, n = 2949) with an average MT length of association of 163 ± 70 nm (±STD, n = 2949). Secondly, we also analyzed the association of non-KMTs with spindle MTs. Non-KMTs showed a similar pattern of increase in the number and length of associations with increasing distances between individual MTs. For a distance of 35 nm, the number of associations was 10 ± 6 (±STD, n = 9957) with an average length of association of 128 ± 75 nm (±STD, n = 9957). With an increase in the distance between MTs, we observed that KMTs tend to show a higher number of associations and a higher average length of associations compared to non-KMTs. Importantly, these results were consistent for all selected association distances, thus confirming that both KMTs and non-KMTs show distinct patterns of MT-MT associations within the metaphase spindle.

bioRxiv preprint doi: https://doi.org/10.1101/2021.11.13.468347; this version posted November 13, 2021. The copyright holder for this preprint (which was not certified by peer review) is the author/funder. All rights reserved. No reuse allowed without permission.

Discussion

The ultrastructure of human k-fibers was insufficiently described prior to this study on the 3D organization of metaphase spindles. Large-scale reconstruction by serial-electron tomography allowed quantitative analyses of KMT organization in individual k-fibers in the context of whole spindles.

Type of kinetochore-to-spindle pole connection

Electron tomography revealed that on average nine KMTs are attached to each kinetochore in HeLa cells in metaphase. This result differs from previous observations in PtK_1 cells (McEwen et al., 1997; O'Toole et al., 2020). In this marsupial cell line, about 20 KMTs were reported to connect to the kinetochores. This difference in the number of attached KMTs could be related to kinetochore size. As previously observed by light microscopy, kinetochores in HeLa cells have about half of the size of kinetochores in PtK_1 cells (Cherry et al., 1989). Similarly, kinetochore size in PtK_1 cells was 0.157 ± 0.045 μm^2 (mean ± STD; (McEwen et al., 1997)) as observed by electron tomography, whereas kinetochores in HeLa cells, as determined indirectly by electron tomography in this study, have an estimated size of about 0.07 ± 0.05 μm^2 (mean ± STD). Possibly, the kinetochore area might indirectly define the size and/or the number of the available free binding sites for MTs (Drpic et al., 2018; Monda and Cheeseman, 2018). The size of the kinetochore appears to be different in different species (Campbell et al., 2019).

We also observed that the connection between kinetochores and the spindle poles is not direct. Textbook models of k-fibers often show KMTs of equal length that are organized in parallel, giving the impression of 'compact rods' connecting kinetochores and spindle poles. This view of the mammalian k-fiber is not consistent with our tomographic data, as k-fibers in our reconstructions show remarkable morphological variability in their circumference along their length (**Fig. 9A**). KMTs in our reconstructed k-fibers are also of different lengths, confirming previous observations (McDonald et al., 1992; O'Toole et al., 2020). In fact, the k-fibers have many short KMTs (less than 1.53 µm in length: see **Fig. 4C**) with their minus ends not positioned near the spindle pole. On the other hand, the pole-to-kinetochore linkage in HeLa cells is also not entirely indirect, as we could only find a small percentage of k-fibers in our reconstructions (about 5%; **Figure 3-figure supplement 1B**) that did not show any KMT associated with the corresponding spindle pole. Thus, our tomographic analysis suggests a semi-direct connection, in which at least one KMT of the k-fibers is directly connected to the poles, while the other KMTs of the fiber are indirectly linked to non-KMTs (**Fig. 9B**).

bioRxiv preprint doi: https://doi.org/10.1101/2021.11.13.468347; this version posted November 13, 2021. The copyright holder for this preprint (which was not certified by peer review) is the author/funder. All rights reserved. No reuse allowed without permission.

KMT organization and interaction with non-KMTs

The length distribution of KMTs in HeLa cells shows striking similarities to the distribution observed in the early *C. elegans* embryo (Redemann et al., 2017). Both human KMTs attached to monocentric kinetochores and also nematode KMTs associated with dispersed holocentric kinetochores show a rather flat length distribution with a smooth cut-off and a rather low number of both very short and very long KMTs. In contrast, non-KMTs in both systems show an exponential length distribution with a very high occurrence of very short microtubules (around 64% of the MTs in HeLa cells were less than 2 µm). This argues that KMTs in both spindles have distinct properties different from non-KMTs.

We observed different association patterns for KMTs *versus* non-KMTs. While both KMTs and non-KMTs showed a clear correlation in the number and the average length of associations (**Figure 8-figure supplement 1**), both MT populations showed differences in the position of these associations. KMTs showed a high tendency to associate with non-KMTs at the spindle poles, and this was independent of the chosen association distance. Our results strongly suggest that KMTs preferably associate with other MTs at the spindle poles, thus achieving an anchoring into the spindle network as previously observed in the early *C. elegans* embryo (Redemann et al., 2017). This anchoring might be promoted by the observed splaying of the k-fibers.

In contrast, non-KMTs showed a flat pattern of interaction with other MTs at association distances of 25 and 35 nm. Moreover, an increase in the association distance from 35 nm to 50 nm, showed a higher tendency of non-KMTs to associate with MTs in the center of the spindle. At the same time, we observed a decrease in the number of associations of KMTs with the MT network at the same position. This is very likely related to the organization of interpolar MTs in the center of the spindle (**Figure 7-figure supplement 1F**) (Kajtez et al., 2016; Mastronarde et al., 1993; Vukušić et al., 2017).

By visual inspection of our reconstructed metaphase spindles, we could indeed observe an apparent association of KMTs with non-KMTs. Our data suggest a stochastic distribution of an association of k-fibers with non-KMTs. However, the 3D organization of interdigitating MTs in the mitotic spindle will be subject to a separate study.

In a parallel study, we have combined our 3D reconstructions with additional live-cell imaging and stochastic simulation (Conway et al., 2021). Therein, we provide evidence for a guided outgrowth of KMTs emanating from kinetochores and present a biophysical model in which the spindle apparatus is considered as a liquid crystal constraining the path of KMT outgrowth towards the spindle poles by neighboring non-KMTs.

bioRxiv preprint doi: https://doi.org/10.1101/2021.11.13.468347; this version posted November 13, 2021. The copyright holder for this preprint (which was not certified by peer review) is the author/funder. All rights reserved. No reuse allowed without permission.

Experimental procedures

Cultivation of cells

HeLa (Kyoto) cells were grown in Dulbecco's Modified Eagle's Medium (DMEM) supplemented with 10% fetal bovine serum (FBS) and 100 units/ml of penicillin/streptomycin (Pen/Strep). Flasks were placed in a humidified incubator at 37°C with a supply of 5% CO_2. For electron microscopy, cells in mitosis were enriched by applying the shake-off technique (Kiewisz et al., 2021). Flasks with cell confluency of 60-80% were shaken against the laboratory bench. The medium with detached cells was then collected, centrifuged at 1200 rpm for 3 min at room temperature, and resuspended in 1 ml of pre-warmed DMEM medium.

Electron tomography

Specimen preparation for electron microscopy

Cultures enriched in mitotic HeLa cells were further processed for electron microscopy essentially as described (Guizetti et al., 2011; Kiewisz et al., 2021). Briefly, sapphire discs with a diameter of 6 mm were cleaned in Piranha solution (1:1 H_2SO_4 and H_2O_2, v/v), coated with poly-L-lysine (0.1% in ddH_2O, w/v) and dried for 2 hrs at 60°C. Furthermore, the discs were coated with fibronectin (1:10 dilution in 1x PBS, v/v) for 2 hrs and were stored in a humidified incubator until further used. The sapphire discs were then placed into custom-designed 3D-printed incubation chambers (Kiewisz et al., 2021). Subsequently, cells were seeded on the coated sapphire discs and incubated for 10 min in a humidified incubator at 37°C supplied with 5% CO_2. This allowed the mitotic cells to re-attach to the surface of the coated sapphire discs and continue to divide.

High-pressure freezing and freeze substitution

Cells were cryo-immobilized using an EM ICE high-pressure freezer (Leica Microsystems, Austria). For each run of freezing, a type-A aluminum carrier (Wohlwend, Switzerland) with the 100 µm-cavity facing up was placed in the specimen loading device of the EM ICE system. The cavity of the type A carrier was then filled with 5 µl of DMEM containing an additional 10% BSA, and the ‘sandwich’ was immediately closed by placing a 6 mm-sapphire disc with attached cells facing down. Finally, a spacer ring was mounted on top of the assembled sample ‘sandwich’ and the freezing was started. Samples were frozen under high pressure (~2000 bar) with a cooling rate of ~20,000 °C/s (Reipert et al., 2004). Frozen samples were then opened under liquid nitrogen and transferred to cryo-vials filled with anhydrous acetone containing 1% (w/v) osmium tetroxide (EMS, USA) and 0.1% (w/v) uranyl acetate

bioRxiv preprint doi: https://doi.org/10.1101/2021.11.13.468347; this version posted November 13, 2021. The copyright holder for this preprint (which was not certified by peer review) is the author/funder. All rights reserved. No reuse allowed without permission.

(Polysciences, USA). Freeze substitution was performed in either a Leica AFS or a Lecia AFS II (Leica Microsystems, Austria). Samples were kept at -90°C for 1 h, warmed up to -30°C with increments of 5 °C/h, kept for 5 hrs at -30°C, and then warmed up to 0°C (increments of 5 °C/h). Finally, samples were allowed to warm up to room temperature. After freeze substitution, samples were washed three times with pure anhydrous acetone and infiltrated with Epon/Araldite (EMS, USA) using increasing concentrations of resin (resin:acetone: 1:3, 1:1, 3:1, then pure resin) for 1 hrs each step at room temperature (Muller-Reichert et al., 2003). Samples were infiltrated with pure resin overnight and then embedded by using commercial flow-through chambers (Leica, Vienna, Austria) designed for sapphire discs of a diameter of 6 mm. Samples were polymerized at 60°C for 36 hrs.

Pre-selection of staged cells

To select cells in metaphase, resin-embedded samples were pre-inspected using an Axiolab RE upright brightfield microscope (Zeiss, Oberkochen, Germany) with a 5x and a 40x objective lens (Zeiss, Oberkochen, Germany). Selected cells in metaphase were sectioned using an EM UC6 ultramicrotome (Leica Microsystems, Austria). Ribbons of semi-thick (~300 nm) serial sections were collected on Formvar-coated copper slot grids, post-stained with 2% (w/v) uranyl acetate in 70% (v/v) methanol, followed by 0.4% (w/v) lead citrate (Science Services, USA) in double-distilled water. In addition, 20 nm colloidal gold (British Biocell International, UK) was attached to the serial sections, serving as fiducial markers for subsequent electron tomography. The selected cells were then pre-inspected at low magnification (~2900x) using either an EM906 (Zeiss, Oberkochen, Germany) or a TECNAI T12 Biotwin (ThermoFisher Scientific, Eindhoven, The Netherlands) transmission electron microscope operated at 80 kV or 120 kV, respectively.

Acquisition and calculation of tomograms

Serial sections of the selected cells were then transferred to a TECNAI F30 transmission electron microscope (ThermoFisher Scientific, Eindhoven, The Netherlands) operated at 300 kV and equipped with a US1000 CCD camera (Gatan, USA). Using a dual-axis specimen holder (Type 2040, Fishione, Export, PA, USA), tilt series were acquired from −65° to +65° with 1° increments at a magnification of 4700x and a final pixel size of 2.32 nm applying the SerialEM software package (Mastronarde, 2005, 2003). For double-tilt electron tomography, the grids were rotated for 90 degrees and the second tilt series were acquired using identical microscope settings (Mastronarde, 1997). The tomographic A- and B-stacks were combined using IMOD (Kremer et al., 1996; Mastronarde and Held, 2017). For each spindle reconstruction, montages of 2 × 3 frames were collected. Depending on the orientation of the

bioRxiv preprint doi: https://doi.org/10.1101/2021.11.13.468347; this version posted November 13, 2021. The copyright holder for this preprint (which was not certified by peer review) is the author/funder. All rights reserved. No reuse allowed without permission.

spindles during the sectioning process, between 22 to 35 serial sections were used to fully reconstruct the volumes of the three selected spindles (**Table 8**).

Segmentation of microtubules and stitching of serial tomograms

As previously published (Redemann et al., 2014; Weber et al., 2012) MTs were automatically segmented using the ZIBAmira (Zuse Institute Berlin, Germany) software package (Stalling et al., 2005). After manual correction of MT segmentation, the serial tomograms of each recorded cell were stitched using the segmented MTs as alignment markers (Lindow et al., 2021). Following this pipeline of data acquisition and 3D reconstruction, three complete models of HeLa cells in metaphase were obtained.

Quantification of tomographic data

For the preparation of the reconstructed mitotic spindles for further quantitative analysis, the ZIBAmira (Zuse Institute Berlin, Germany) software package was used (Stalling et al., 2005). In addition, an automatic spatial graph analysis (ASGA) software tool was created for the quantification of the tomographic data (Kiewisz and Müller-Reichert, 2021). In detail, we analyzed the length and minus end distribution of KMTs. Furthermore, we quantified the position of each k-fiber in the mitotic spindles followed by an analysis of the tortuosity, the cross-section area, the shape and the density of k-fibers.

Staging of spindles

For a precise staging of the three reconstructed metaphase spindles, we determined the inter-kinetochore distance. For this, the closest neighboring sister kinetochores were determined. The center of each kinetochore was then defined as a median position of all KMT plus ends associated with each selected kinetochore, and the inter-kinetochore distance was then calculated as the 3D Euclidean distance between the defined median centers of each kinetochore pair. For each mitotic spindle, the inter-kinetochore distance is given as the mean value (mean ± standard deviation, STD). As an additional criterion for mitotic staging, the pole-to-pole distances were measured. For this, we measured the 3D Euclidean distance between the centers of the manually segmented mother centrioles in each data set. This read-out was used to determine the spindle size at metaphase.

Classification of MTs

MTs with their putative plus end associated with the chromosomes were defined as KMTs. Characteristically, these KMTs showed a parallel arrangement at the site of attachment to the chromosomes. Unfortunately, identification of individual kinetochores in our electron

bioRxiv preprint doi: https://doi.org/10.1101/2021.11.13.468347; this version posted November 13, 2021. The copyright holder for this preprint (which was not certified by peer review) is the author/funder. All rights reserved. No reuse allowed without permission.

tomograms was hindered by the fact that prominent electron-dense monopolar KMT attachment sites, as described previously for conventionally fixed cells (McEwen et al., 1998), were not always clearly visible after cryo-fixation by high-pressure freezing. All other MTs in the 3D reconstructions were classified as non-KMTs.

MT - centrosome interaction area estimation

The KMT minus end distance to the closest spindle pole was calculated as a 3D Euclidean distance. The border of the spindle pole (the MT - centrosome interaction area) was estimated from all data sets by defining a distribution peak of non-KMT minus end distance to a spindle pole. The centrosome interaction area was then defined as a double of half-width from the distribution peak.

Length distribution of MTs

The full length of each reconstructed KMT and non-KMTs was measured, and the average is given for each data set (mean ± STD). We also analyzed the percentage of short versus long KMTs. For each data set, short KMTs were defined as those shorter than 1.53 µm in length. This threshold was chosen based on the MT - centrosome interaction area. The long KMTs were identified as KMTs longer than a half-spindle length for each given data set.

Position of MT minus ends

To analyze the position of the KMT minus ends in the metaphase spindles, the 3D Euclidean distance of each KMT minus end to the closest spindle pole (i.e., to the center of the mother centriole) was determined. In addition, the relative position of KMT minus ends along the pole-to-kinetochore axis was calculated. The relative position of each minus end is given as the normalized position between the kinetochore (position = 1) and mother centriole (position = 0) along the spindle axis. The distribution of relative positions of KMT minus ends (mean, ± STD) is given for each data set. The number of KMT minus ends not associated with the spindle pole were defined as minus ends detected further than the calculated MT - centrosome interaction area.

Interaction of KMTs with non-KMTs

KMT minus ends association with other MT lattices was calculated as a 3D Euclidean distance. For that firstly, KMT minus ends were identified as KMT ends that were closer to one of the spindle poles. Finally, a possible association between KMT ends and other MT lattices was measured by calculating a 3D Euclidean distance between KMT ends and every MT lattice in the reconstructed spindle. The interaction between KMT minus ends and MT lattice was identified if KMT minus ends were found in interaction distance to any MT lattice. The

bioRxiv preprint doi: https://doi.org/10.1101/2021.11.13.468347; this version posted November 13, 2021. The copyright holder for this preprint (which was not certified by peer review) is the author/funder. All rights reserved. No reuse allowed without permission.

interaction distance was defined as 25, 30, 35, 45, 50, 75 and 100 nm. For visualization, each KMT was labeled based on the type of detected interaction (no interaction, interaction with KMT, interaction with non-KMT). The percentage number of KMT with any interaction was measured and the average value for all data sets is given (mean ± STD).

Additionally, to identify possible MT minus ends association with KMT lattices, the 3D Euclidean distances of the MT minus ends to KMT lattices were calculated. The association between KMT lattices and MT minus ends was identified if MT minus ends were found in interaction distance to KMT lattices. The interaction distance was defined as 25, 30, 35, 45, 50, 75 and 100 nm. The percentage number of KMT with any interaction was measured and the average from all datasets is given (mean ± STD). Moreover, to calculate the position on the KMT where the interaction occurred, a relative position of MT minus ends on the pole-to-kinetochore axis was calculated. The relative position of each minus end is given as the normalized position between the kinetochore (position = 1) and mother centriole (position = 0) along the spindle axis.

Defining kinetochore position

In order to determine the position of the k-fiber in the mitotic spindle, a position model was created based on the kinetochore localization on the metaphase plate. First, kinetochores were assigned to the outer, middle, or inner regions of the metaphase plate. For that, all kinetochores were projected in a 2D space using an X/Z spindle axis, and an ellipse was fitted into all projected kinetochores in a way that a semi-major axis was defined as the length of the furthest kinetochore on the X-axis, and a semi-minor axis defined as the length of the furthest kinetochore on the Z-axis. The fitted ellipse was divided into three regions ranging from 100 - 75% (outer region), from 75 - 50 % (middle region) and from 50 - 0% (inner region). Kinetochores with associated k-fibers were then assigned to these regions.

Global tortuosity of KMTs

For the analysis of KMT tortuosity, the ratio of the KMT spline length and the 3D Euclidean distance between the plus and the minus end for each KMT was measured. The distribution of KMTs tortuosity (mean, ± STD) is given. In addition, the correlation of the KMT tortuosity with its length is given as a fitted polynomial line calculated as local polynomial regression by the locally estimated scatterplot smoothing “loess” method. A confidence interval for the created polynomial line was calculated with the t-based approximation which is defined as the overall uncertainty of how the fitted polynomial line fits the population of all data points. Local polynomial regressions and confidence intervals for all data sets were calculated using the stat 4.0.3 R library (R Core Team, 2021).

bioRxiv preprint doi: https://doi.org/10.1101/2021.11.13.468347; this version posted November 13, 2021. The copyright holder for this preprint (which was not certified by peer review) is the author/funder. All rights reserved. No reuse allowed without permission.

Local tortuosity of KMTs

For the calculation of the local tortuosity, each KMT was subsampled with segments of a length of 500 nm. Both the tortuosity and the relative position along the pole-to-kinetochore axis were measured for each segment. In addition, the correlation of local KMT tortuosity against the relative position is given. Local polynomial regressions and confidence intervals for all data sets were calculated using the stat 4.0.3 R library (R Core Team, 2021).

Polygon cross-section area of k-fibers

The cross-section area was calculated every 500 nm along each k-fiber. For each defined cross-section, KMTs position was mapped on a 2D plane, and a polygon shape of a k-fiber cross-section was calculated based on the position of the KMTs. The polygon shape was calculated with the alpha shape algorithm (α = 10) using the “ashape3d” function of the alphashape3d 1.3.1 R library (Lafarge and Pateiro-Lopez, 2020). The alpha shape is the polygon shape formed around a given set of points (KMTs from a cross-section) created by carving space around those points with a circle of a radius defined as α. The polygon shape was then built by drawing outline polygon lines between contact points on the fitted circle. In order to calculate the polygon area from the polygon shape of the k-fiber cross-section, a polygon prism was created by duplicating and shifting a polygon shape 1 µm in the XYZ dimension. This creates a prism with a height of 1 µm. The volume of created 3D object (prism) was then calculated with alphashape3d 1.3.1 R library (Lafarge and Pateiro-Lopez, 2020) and from this, a polygon area could be calculated by dividing the prism volume (V_{pp}) by prism high (h_{pp} = 1 µm). The distribution of the k-fiber polygon area along the pole-to-kinetochore axis is given as a fitted polynomial line of local polynomial regression using the “loess” method and confidence intervals were calculated with the t-based approximation using the stat 4.0.3 R library (R Core Team, 2021).

Density of KMTs in k-fibers

Also, the density of KMTs in the k-fibers was calculated in segments of 500 nm length along the entire path of each fiber. To determine the percentage of KMTs that were enclosed in the k-fiber for each cross-section, the number of KMTs enclosed in the given k-fiber section and circular area were determined. The radius of the circular area was calculated for each k-fiber at the position of the KMTs attached to the kinetochores. The distribution of the k-fiber density along the pole-to-pole axis is given as a fitted polynomial line and a confidence interval calculated with the t-based approximation using the stat 4.0.3 R library (R Core Team, 2021).

Neighborhood analysis of KMT-KMT distances

bioRxiv preprint doi: https://doi.org/10.1101/2021.11.13.468347; this version posted November 13, 2021. The copyright holder for this preprint (which was not certified by peer review) is the author/funder. All rights reserved. No reuse allowed without permission.

The neighborhood KMTs at a given k-fiber cross-section were selected by K-nearest neighbor estimation. The estimation was achieved by firstly calculating a distance matrix between all selected KMTs. Given a distance matrix, each KMT-KMT connection was ranked according to its distance. Finally, for each KMT in a k-fiber, neighboring KMTs were selected by picking KMTs with k=1. For each k-fiber, a mean KMT-KMT neighborhood distance and standard deviation were calculated.

Interaction of MTs

The interaction between MTs was calculated for every 20 nm segment along each MT. For that, for each MT segment, a distance to neighboring MTs was calculated. The MT-MT interaction was defined if any given MT segment were closer or at an interaction distance. The interaction distance between MTs was defined as 25, 30, 35, 45, 50 nm. For visualization, each MT segment was labeled based on the number of interactions. The length of interaction between MTs was calculated as a sum of 20 nm segments. The frequency plot of average MT interaction length and average interaction per MT was given for each interaction distance.

Custom-designed software for the visualization of 3D data

To better understand the 3D organization of KMTs in k-fibers, a visualization platform was developed using the WebGL library (rgl 0.106.8 R library; (Adler et al., 2021)). This platform was implemented for the public. This novel tool will allow readers to choose data sets from this publication and visualize spindles according to selected features in an interactive way. For instance, users may choose to visualize the organization of k-fibers or KMTs, and select for the analysis of MT-MT. For an analysis of KMTs, users can select the following features of analysis: length distribution, minus end positioning, curvature, and KMT number at the kinetochore along with others. For the MT-MT interaction analysis, users can select different interaction distances. This platform is designed to continuously add 3D reconstructions of spindles obtained from different systems and can be accessed as follows: https://cfci.shinyapps.io/ASGA_3DViewer/.

bioRxiv preprint doi: https://doi.org/10.1101/2021.11.13.468347; this version posted November 13, 2021. The copyright holder for this preprint (which was not certified by peer review) is the author/funder. All rights reserved. No reuse allowed without permission.

Data availability

Tomographic data has been uploaded to the TU Dresden Open Access Repository and Archive system (OpARA) and is available as open access: http://doi.org/10.25532/OPARA-128

The code used to perform quantitative analysis of MT organization in spindles has been uploaded to the GitHub repository and is available as open access under the GPL v3.0 license: https://github.com/RRobert92/ASGA

Acknowledgments

The authors would like to thank Dr. Tobias Fürstenhaupt (Electron Microscopy Facility at the MPI-CBG, Dresden, Germany) for technical support. We are also grateful to Drs. Reza Farhadifar, Stefanie Redemann, Alejandra Laguillo Diego and Isabelle Vernos for a critical reading of the manuscript. Research in the Müller-Reichert laboratory is supported by funds from the Deutsche Forschungsgemeinschaft (MU 1423/8-2). R.K. received funding from the European Union's Horizon 2020 research and innovation program under the Marie Skłodowska-Curie grant agreement No. 675737 (grant to T.M.R.). This work was supported by the NSF-Simons Center for Mathematical and Statistical Analysis of Biology at Harvard (award number #1764269), and the Harvard Quantitative Biology Initiative.

Declaration of interests

The authors declare no competing financial interests.

bioRxiv preprint doi: https://doi.org/10.1101/2021.11.13.468347; this version posted November 13, 2021. The copyright holder for this preprint (which was not certified by peer review) is the author/funder. All rights reserved. No reuse allowed without permission.

References

Adler D, Murdoch D, Nenadic O, Urbanek S, Chen M, Gebhardt A, Bolker B, Csardi G, Srzelecki A, Senger A. 2021. RGL - 3D visualization device system for R using OpenGL.

Amos LA. 1989. Brain dynein crossbridges microtubules into bundles. *J Cell Sci* **93**:19–28.

Anjur-Dietrich MI, Kelleher CP, Needleman DJ. 2021. Mechanical Mechanisms of Chromosome Segregation. *Cells* **10**:465. doi:10.3390/cells10020465

Begley MA, Solon AL, Davis EM, Sherrill MG, Ohi R, Elting MW. 2021. K-fiber bundles in the mitotic spindle are mechanically reinforced by Kif15. *Mol Biol Cell* **32**:2020.05.19.104661. doi:10.1091/mbc.E20-06-0426

Campbell S, Amin MA, Varma D, Bidone TC. 2019. Computational model demonstrates that Ndc80-associated proteins strengthen kinetochore-microtubule attachments in metaphase. *Cytoskeleton* **76**:549–561. doi:10.1002/cm.21562

Cherry LM, Faulkner AJ, Grossberg LA, Balczon R. 1989. Kinetochore size variation in mammalian chromosomes: an image analysis study with evolutionary implications. *J Cell Sci* **92**:281–289.

Conway W, Kiewisz R, Fabig G, Kelleher, Colm, Wu, Hai-Yin, Anjur-Dietrich, Maya, Müller-Reichert T, Needleman DJ. 2021. Self-organization of kinetochore-fibers in human mitotic spindles. *bioRxiv*.

DeLuca JG, Gall WE, Ciferri C, Cimini D, Musacchio A, Salmon ED. 2006. Kinetochore Microtubule Dynamics and Attachment Stability Are Regulated by Hec1. *Cell* **127**:969–982. doi:10.1016/j.cell.2006.09.047

Drpic D, Almeida AC, Aguiar P, Renda F, Damas J, Lewin HA, Larkin DM, Khodjakov A, Maiato H. 2018. Chromosome Segregation Is Biased by Kinetochore Size. *Curr Biol* **28**:1344-1356.e5. doi:10.1016/j.cub.2018.03.023

Dumont S, Mitchison TJ. 2009. Force and Length in the Mitotic Spindle. *Curr Biol* **19**:749–761. doi:10.1016/j.cub.2009.07.028

Fabig G, Kiewisz R, Lindow N, Powers JA, Cota V, Quintanilla LJ, Brugués J, Prohaska S, Chu DS, Müller-Reichert T. 2020. Male meiotic spindle features that efficiently segregate paired and lagging chromosomes. *elife* **9**. doi:10.7554/eLife.50988

Falnikar A, Tole S, Baas PW. 2011. Kinesin-5, a mitotic microtubule-associated motor protein,

bioRxiv preprint doi: https://doi.org/10.1101/2021.11.13.468347; this version posted November 13, 2021. The copyright holder for this preprint (which was not certified by peer review) is the author/funder. All rights reserved. No reuse allowed without permission.

modulates neuronal migration. *Mol Biol Cell* **22**:1561–1574. doi:10.1091/mbc.e10-11-0905

Farhadifar R, Yu C-H, Fabig G, Wu H-Y, Stein DB, Rockman M, Müller-Reichert T, Shelley MJ, Needleman DJ. 2020. Stoichiometric interactions explain spindle dynamics and scaling across 100 million years of nematode evolution. *elife* **9**:1–26. doi:10.7554/eLife.55877

Flemming W. 1879. Beitrage zur Kenntniss der Zelle und ihrer Lebenserscheinungen. *Arch für Mikroskopische Anat* **16**:302–436. doi:10.1007/BF02956386

Godek KM, Kabeche L, Compton DA. 2015. Regulation of kinetochore–microtubule attachments through homeostatic control during mitosis. *Nat Rev Mol Cell Biol* **16**:57–64. doi:10.1038/nrm3916

Guizetti J, Schermelleh L, Mäntler J, Maar S, Poser I, Leonhardt H, Müller-Reichert T, Gerlich DW. 2011. Cortical Constriction During Abscission Involves Helices of ESCRT-III–Dependent Filaments. *Science* **331**:1616–1620. doi:10.1126/science.1201847

Hoffman DP, Shtengel G, Xu CS, Campbell KR, Freeman M, Wang L, Milkie DE, Pasolli HA, Iyer N, Bogovic JA, Stabley DR, Shirinifard A, Pang S, Peale D, Schaefer K, Pomp W, Chang C-L, Lippincott-Schwartz J, Kirchhausen T, Solecki DJ, Betzig E, Hess HF. 2020. Correlative three-dimensional super-resolution and block-face electron microscopy of whole vitreously frozen cells. *Science* **367**:eaaz5357. doi:10.1126/science.aaz5357

Inoué S. 1953. Polarization optical studies of the mitotic spindle. *Chromosoma* **5**:487–500. doi:10.1007/BF01271498

Inoué S, Salmon ED. 1995. Force Generation by Microtubule Assembly/Disassembly in Mitosis and Related Movements. *Mol Biol Cell* **6**:1619–1640. doi:10.1091/mbc.6.12.1619

Kajtez J, Solomatina A, Novak M, Polak B, Vukušić K, Rüdiger J, Cojoc G, Milas A, Šumanovac Šestak I, Risteski P, Tavano F, Klemm AH, Roscioli E, Welburn J, Cimini D, Glunčić M, Pavin N, Tolić IM. 2016. Overlap microtubules link sister k-fibres and balance the forces on bi-oriented kinetochores. *Nat Commun* **7**:10298. doi:10.1038/ncomms10298

Khodjakov A, Cole RW, McEwen BF, Buttle KF, Rieder CL. 1997. Chromosome Fragments Possessing Only One Kinetochore Can Congress to the Spindle Equator. *J Cell Biol* **136**:229–240. doi:10.1083/jcb.136.2.229

bioRxiv preprint doi: https://doi.org/10.1101/2021.11.13.468347; this version posted November 13, 2021. The copyright holder for this preprint (which was not certified by peer review) is the author/funder. All rights reserved. No reuse allowed without permission.

Kiewisz R, Müller-Reichert T. 2021. Automatic Spatial-Graph Analysis (ASGA). doi:https://doi.org/10.5281/zenodo.3732108

Kiewisz R, Müller-Reichert T, Fabig G. 2021. High-throughput screening of mitotic mammalian cells for electron microscopy using classic histological dyes In: Müller-Reichert T, Verkade P, editors. Methods in Cell Biology:Correlative Light and Electron Microscopy IV. New Jersey: Academic Press Inc. pp. 151–170. doi:10.1016/bs.mcb.2020.08.005

Kremer JR, Mastronarde DN, McIntosh JR. 1996. Computer Visualization of Three-Dimensional Image Data Using IMOD. *J Struct Biol* **116**:71–76. doi:10.1006/jsbi.1996.0013

Kuhn J, Dumont S. 2019. Mammalian kinetochores count attached microtubules in a sensitive and switch-like manner. *J Cell Biol* **218**:3583–3596. doi:10.1083/jcb.201902105

Lafarge T, Pateiro-Lopez B. 2020. alphashape3d: Implementation of the 3D Alpha-Shape for the Reconstruction of 3D Sets from a Point Cloud.

Lindow N, Brünig FN, Dercksen VJ, Fabig G, Kiewisz R, Redemann S, Müller-Reichert T, Prohaska S, Baum D. 2021. Semi-automatic stitching of filamentous structures in image stacks from serial-section electron tomography. *J Microsc* **284**:25–44. doi:10.1111/jmi.13039

Long AF, Suresh P, Dumont S. 2020. Individual kinetochore-fibers locally dissipate force to maintain robust mammalian spindle structure. *J Cell Biol* **219**:1–13. doi:10.1083/jcb.201911090

Maiato H, Rieder CL, Khodjakov A. 2004. Kinetochore-driven formation of kinetochore fibers contributes to spindle assembly during animal mitosis. *J Cell Biol* **167**:831–840. doi:10.1083/jcb.200407090

Mastronarde DN. 2005. Automated electron microscope tomography using robust prediction of specimen movements. *J Struct Biol* **152**:36–51. doi:10.1016/j.jsb.2005.07.007

Mastronarde DN. 2003. SerialEM: A Program for Automated Tilt Series Acquisition on Tecnai Microscopes Using Prediction of Specimen Position. *Microsc Microanal* **9**:1182–1183. doi:10.1017/S1431927603445911

Mastronarde DN. 1997. Dual-Axis Tomography: An Approach with Alignment Methods That Preserve Resolution. *J Struct Biol* **120**:343–352. doi:10.1006/jsbi.1997.3919

Mastronarde DN, Held SR. 2017. Automated tilt series alignment and tomographic

bioRxiv preprint doi: https://doi.org/10.1101/2021.11.13.468347; this version posted November 13, 2021. The copyright holder for this preprint (which was not certified by peer review) is the author/funder. All rights reserved. No reuse allowed without permission.

reconstruction in IMOD. *J Struct Biol* **197**:102–113. doi:10.1016/j.jsb.2016.07.011

Mastronarde DN, McDonald KL, Ding R, McIntosh JR. 1993. Interpolar spindle microtubules in PTK cells. *J Cell Biol* **123**:1475–1489. doi:10.1083/jcb.123.6.1475

McDonald KL, O'Toole ET, Mastronarde DN, McIntosh JR. 1992. Kinetochore microtubules in PTK cells. *J Cell Biol* **118**:369–383. doi:10.1083/jcb.118.2.369

McEwen BF, Ding Y, Heagle AB. 1998. Relevance of kinetochore size and microtubule-binding capacity for stable chromosome attachment during mitosis in PtK1 cells. *Chromosom Res* **6**:123–132. doi:10.1023/A:1009239013215

McEwen BF, Heagle AB, Cassels GO, Buttle KF, Rieder CL. 1997. Kinetochore Fiber Maturation in PtK1 Cells and Its Implications for the Mechanisms of Chromosome Congression and Anaphase Onset. *J Cell Biol* **137**:1567–1580. doi:10.1083/jcb.137.7.1567

McIntosh JR, O'Toole E, Zhudenkov K, Morphew M, Schwartz C, Ataullakhanov FI, Grishchuk EL. 2013. Conserved and divergent features of kinetochores and spindle microtubule ends from five species. *J Cell Biol* **200**:459–474. doi:10.1083/jcb.201209154

Metzner R. 1894. Beitrage zur Granulalehre. I. Kern und kerntheilung. *Arch Anat Physiol* 309–348.

Mitchison T, Kirschner M. 1984. Dynamic instability of microtubule growth. *Nature* **312**:237–242. doi:10.1038/312237a0

Molodtsov MI, Mieck C, Dobbelaere J, Dammermann A, Westermann S, Vaziri A. 2016. A Force-Induced Directional Switch of a Molecular Motor Enables Parallel Microtubule Bundle Formation. *Cell* **167**:539-552.e14. doi:10.1016/j.cell.2016.09.029

Monda JK, Cheeseman IM. 2018. The kinetochore–microtubule interface at a glance. *J Cell Sci* **131**. doi:10.1242/jcs.214577

Muller-Reichert T, Hohenberg H, O'Toole ET, Mcdonald K. 2003. Cryoimmobilization and three-dimensional visualization of C. elegans ultrastructure. *J Microsc* **212**:71–80. doi:10.1046/j.1365-2818.2003.01250.x

Musacchio A, Desai A. 2017. A Molecular View of Kinetochore Assembly and Function. *Biology (Basel)* **6**:5. doi:10.3390/biology6010005

Nixon FM, Gutiérrez-Caballero C, Hood FE, Booth DG, Prior IA, Royle SJ. 2015. The mesh is

bioRxiv preprint doi: https://doi.org/10.1101/2021.11.13.468347; this version posted November 13, 2021. The copyright holder for this preprint (which was not certified by peer review) is the author/funder. All rights reserved. No reuse allowed without permission.

a network of microtubule connectors that stabilizes individual kinetochore fibers of the mitotic spindle. *elife* **4**:1–21. doi:10.7554/eLife.07635

Nixon FM, Honnor TR, Clarke NI, Starling GP, Beckett AJ, Johansen AM, Brettschneider JA, Prior IA, Royle SJ. 2017. Microtubule organization within mitotic spindles revealed by serial block face scanning EM and image analysis. *J Cell Sci* **130**:1845–1855. doi:10.1242/jcs.203877

O'Toole E, Morphew M, McIntosh JR. 2020. Electron tomography reveals aspects of spindle structure important for mechanical stability at metaphase. *Mol Biol Cell* **31**:184–195. doi:10.1091/mbc.E19-07-0405

O'Toole ET, McDonald KL, Mäntler J, McIntosh JR, Hyman AA, Müller-Reichert T. 2003. Morphologically distinct microtubule ends in the mitotic centrosome of Caenorhabditis elegans. *J Cell Biol* **163**:451–456. doi:10.1083/jcb.200304035

Oriola D, Needleman DJ, Brugués J. 2018. The Physics of the Metaphase Spindle. *Annu Rev Biophys* **47**:655–673. doi:10.1146/annurev-biophys-060414-034107

Prosser SL, Pelletier L. 2017. Mitotic spindle assembly in animal cells: A fine balancing act. *Nat Rev Mol Cell Biol*. doi:10.1038/nrm.2016.162

R Core Team. 2021. R: A language and environment for statistical computing. R Foundation for Statistical Computing.

Redemann S, Baumgart J, Lindow N, Shelley M, Nazockdast E, Kratz A, Prohaska S, Brugués J, Fürthauer S, Müller-Reichert T. 2017. C. elegans chromosomes connect to centrosomes by anchoring into the spindle network. *Nat Commun* **8**:15288. doi:10.1038/ncomms15288

Redemann S, Weber B, Möller M, Verbavatz J-M, Hyman AA, Baum D, Prohaska S, Müller-Reichert T. 2014. The Segmentation of Microtubules in Electron Tomograms Using Amira In: Sharp DJ, editor. Mitosis: Methods and Protocols, Methods in Molecular Biology. New York: Springer Science+ Business Media. pp. 261–278. doi:10.1007/978-1-4939-0329-0_12

Reipert S, Fischer I, Wiche G. 2004. High-pressure freezing of epithelial cells on sapphire coverslips. *J Microsc* **213**:81–85. doi:10.1111/j.1365-2818.2004.01260.x

Rieder CL. 1981. The structure of the cold-stable kinetochore fiber in metaphase PtK1 cells. *Chromosoma* **84**:145–158. doi:10.1007/BF00293368

bioRxiv preprint doi: https://doi.org/10.1101/2021.11.13.468347; this version posted November 13, 2021. The copyright holder for this preprint (which was not certified by peer review) is the author/funder. All rights reserved. No reuse allowed without permission.

Rieder CL, Salmon ED. 1998. The vertebrate cell kinetochore and its roles during mitosis. *Trends Cell Biol* **8**:310.

Ris H, Witt PL. 1981. Structure of the mammalian kinetochore. *Chromosoma* **82**:153–170. doi:10.1007/BF00286101

Rosselló C, Lindström L, Eklund G, Corvaisier M, Kristensson M. 2018. γ-Tubulin–γ-Tubulin Interactions as the Basis for the Formation of a Meshwork. *Int J Mol Sci* **19**:3245. doi:10.3390/ijms19103245

Schmidt WJ. 1939. Doppelbrechung der Kernspindel und Zugfasertheorie der Chromosomenbewegung. *Chromosoma* **1**:253–264. doi:10.1007/BF01271634

Sikirzhytski V, Magidson V, Steinman JB, He J, Le Berre M, Tikhonenko I, Ault JG, McEwen BF, Chen JK, Sui H, Piel M, Kapoor TM, Khodjakov A. 2014. Direct kinetochore–spindle pole connections are not required for chromosome segregation. *J Cell Biol* **206**:231–243. doi:10.1083/jcb.201401090

Sikirzhytski V, Renda F, Tikhonenko I, Magidson V, McEwen BF, Khodjakov A. 2018. Microtubules assemble near most kinetochores during early prometaphase in human cells. *J Cell Biol* **217**:2647–2659. doi:10.1083/jcb.201710094

Stalling D, Westerhoff M, Hege H-C. 2005. Amira: a Highly Interactive System for Visual Data Analysis In: Hansen CD, Johnson CR, editors. The Visualization Handbook. Elsevier. pp. 749–767.

Tan R, Foster PJ, Needleman DJ, McKenney RJ. 2018. Cooperative Accumulation of Dynein-Dynactin at Microtubule Minus-Ends Drives Microtubule Network Reorganization. *Dev Cell* **44**:233-247.e4. doi:10.1016/j.devcel.2017.12.023

Vukušić K, Buđa R, Bosilj A, Milas A, Pavin N, Tolić IM. 2017. Microtubule Sliding within the Bridging Fiber Pushes Kinetochore Fibers Apart to Segregate Chromosomes. *Dev Cell* **43**:11-23.e6. doi:10.1016/j.devcel.2017.09.010

Weber B, Greenan G, Prohaska S, Baum D, Hege H-C, Müller-Reichert T, Hyman AA, Verbavatz J-M. 2012. Automated tracing of microtubules in electron tomograms of plastic embedded samples of Caenorhabditis elegans embryos. *J Struct Biol* **178**:129–138. doi:10.1016/j.jsb.2011.12.004

Winey M, Mamay CL, O'Toole ET, Mastronarde DN, Giddings TH, McDonald KL, McIntosh JR. 1995. Three-dimensional ultrastructural analysis of the Saccharomyces cerevisiae

bioRxiv preprint doi: https://doi.org/10.1101/2021.11.13.468347; this version posted November 13, 2021. The copyright holder for this preprint (which was not certified by peer review) is the author/funder. All rights reserved. No reuse allowed without permission.

mitotic spindle. *J Cell Biol* **129**:1601–1615. doi:10.1083/jcb.129.6.1601

bioRxiv preprint doi: https://doi.org/10.1101/2021.11.13.468347; this version posted November 13, 2021. The copyright holder for this preprint (which was not certified by peer review) is the author/funder. All rights reserved. No reuse allowed without permission.

Figures

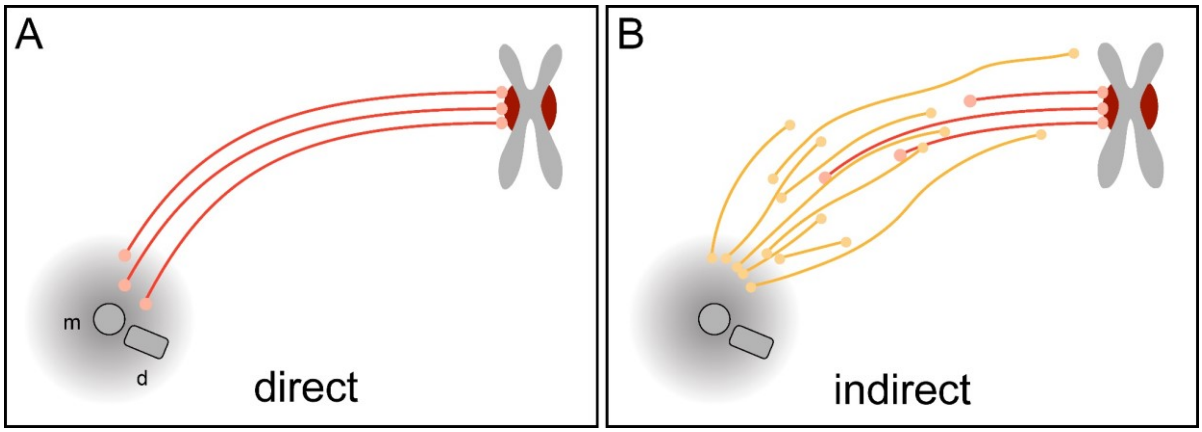

Figure 1. Proposed models on the organization of k-fibers in mammalian mitosis

(A) Direct connection with KMTs (red lines) spanning the distance between the kinetochore and the spindle pole. The mother (m) and the daughter centriole (d) of the centrosome are indicated. All KMTs are assumed to have the same length. **(B)** Indirect connection showing KMTs linking the kinetochore and the centrosome by non-KMTs (yellow lines). K-fibers in this model are composed of KMTs with different lengths, and none of the KMTs is directly associated with the spindle pole.

bioRxiv preprint doi: https://doi.org/10.1101/2021.11.13.468347; this version posted November 13, 2021. The copyright holder for this preprint (which was not certified by peer review) is the author/funder. All rights reserved. No reuse allowed without permission.

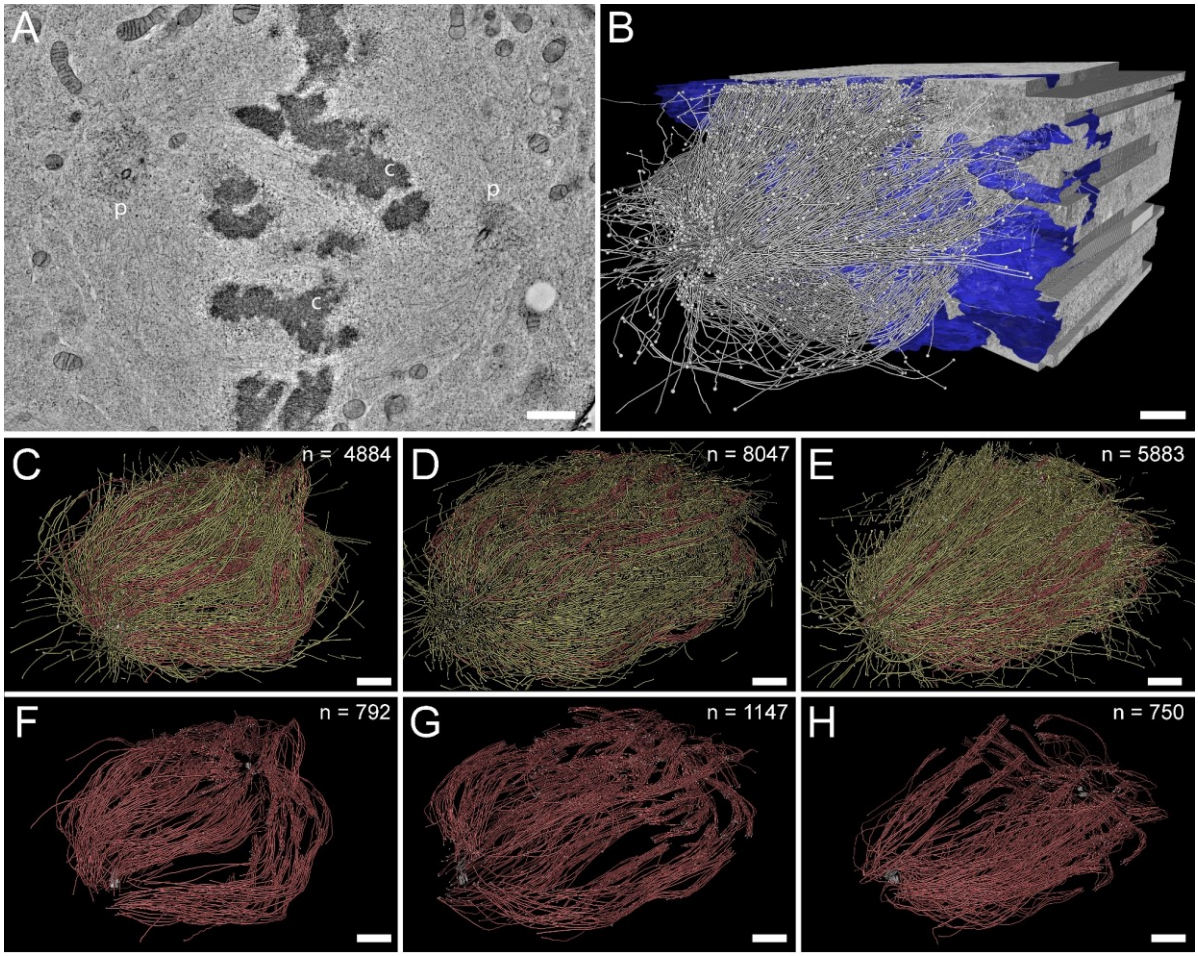

Figure 2. Three-dimensional reconstruction of metaphase spindles by large-scale electron tomography

(**A**) Tomographic slice showing a HeLa cell (spindle #1) in metaphase at low magnification. The chromosomes (c) and the spindle poles (p) are indicated. (**B**) Three-dimensional reconstruction of the spindle in the same cell as shown in A. The stitching of the serial tomograms to generate a three-dimensional model of the spindle with the MTs (white lines) is illustrated. The segmented chromosomes are shown in blue. (**C**) Three-dimensional model of the spindle as shown in A. The total number of microtubules is indicated (upper left corner). The non-KMTs (yellow lines) and KMTs (red lines) are shown. (**D**) Full 3D model of metaphase spindle #2. (**E**) Full 3D model of metaphase spindle #3. (**F**) Extraction of KMTs from the 3D reconstruction as shown in C. The number of KMTs for this spindle is indicated. (**G**) KMTs extracted from spindle #2. (**H**) KMTs extracted from spindle #3. Scale bars, 1 µm.

bioRxiv preprint doi: https://doi.org/10.1101/2021.11.13.468347; this version posted November 13, 2021. The copyright holder for this preprint (which was not certified by peer review) is the author/funder. All rights reserved. No reuse allowed without permission.

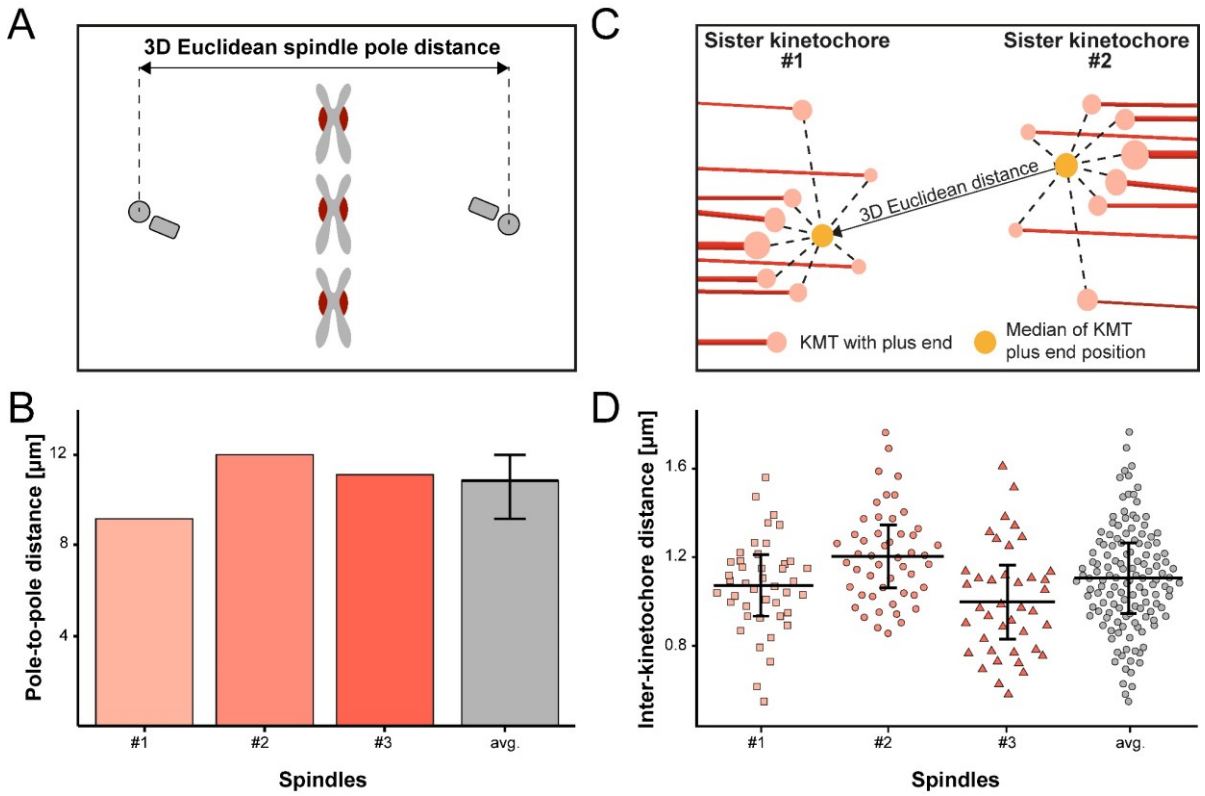

Figure 2. Three-dimensional reconstruction of metaphase spindles by large-scale electron tomography

(**A**) Tomographic slice showing a HeLa cell (spindle #1) in metaphase at low magnification. The chromosomes (c) and the spindle poles (p) are indicated. (**B**) Three-dimensional reconstruction of the spindle in the same cell as shown in A. The stitching of the serial tomograms to generate a three-dimensional model of the spindle with the MTs (white lines) is illustrated. The segmented chromosomes are shown in blue. (**C**) Three-dimensional model of the spindle as shown in A. The total number of microtubules is indicated (upper left corner). The non-KMTs (yellow lines) and KMTs (red lines) are shown. (**D**) Full 3D model of metaphase spindle #2. (**E**) Full 3D model of metaphase spindle #3. (**F**) Extraction of KMTs from the 3D reconstruction as shown in C. The number of KMTs for this spindle is indicated. (**G**) KMTs extracted from spindle #2. (**H**) KMTs extracted from spindle #3. Scale bars, 1 µm.

bioRxiv preprint doi: https://doi.org/10.1101/2021.11.13.468347; this version posted November 13, 2021. The copyright holder for this preprint (which was not certified by peer review) is the author/funder. All rights reserved. No reuse allowed without permission.

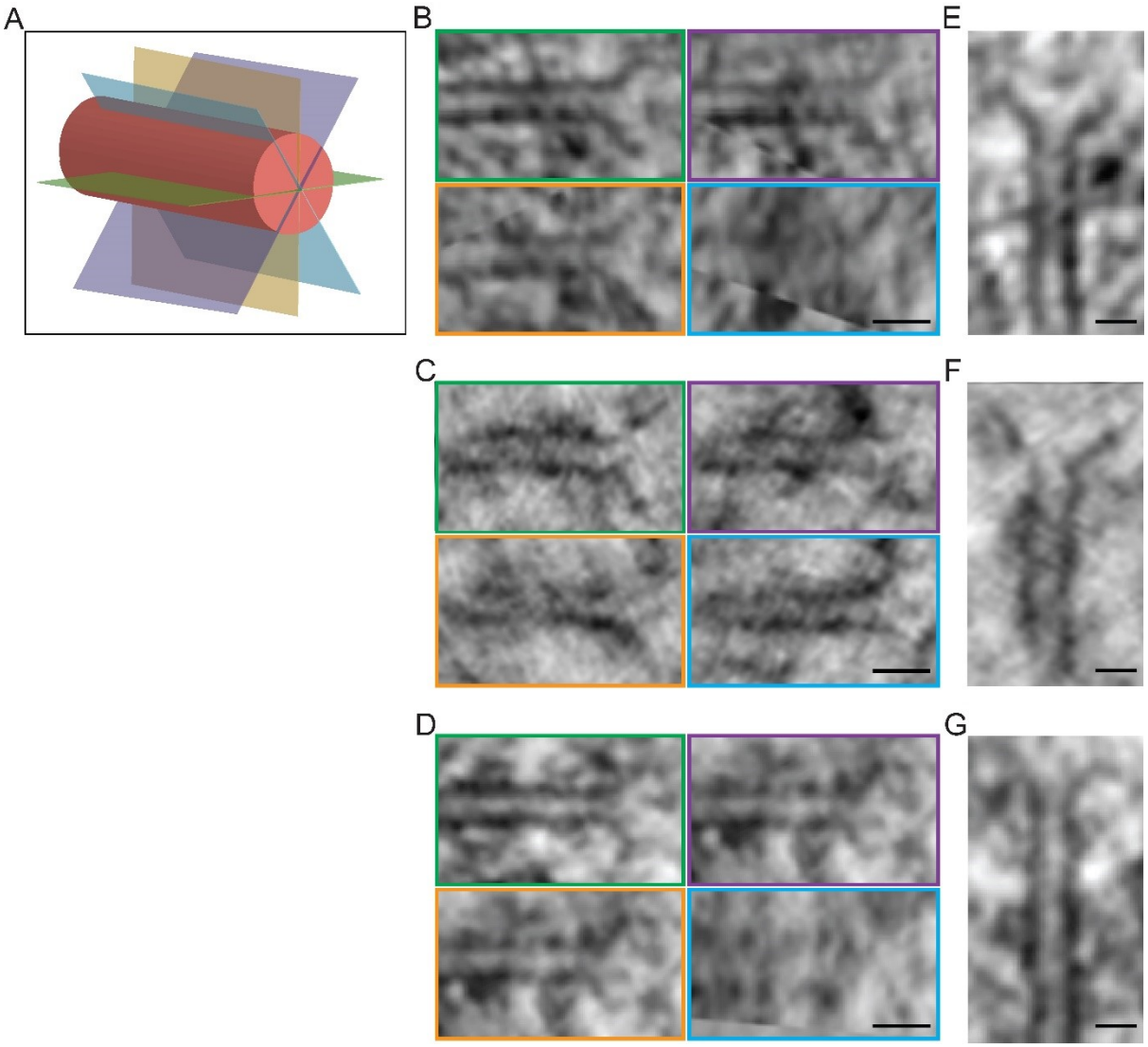

Figure 2-figure supplement 2. Selection of KMT plus ends based on end morphology

(**A**) Schematic illustration of MT cross-sections as used to visualize the end morphology of KMTs. (**B-D**) Cross-sections of KMT plus ends as shown in A. (**E-G**) Average intensity z-projection of KMT plus ends.

bioRxiv preprint doi: https://doi.org/10.1101/2021.11.13.468347; this version posted November 13, 2021. The copyright holder for this preprint (which was not certified by peer review) is the author/funder. All rights reserved. No reuse allowed without permission.

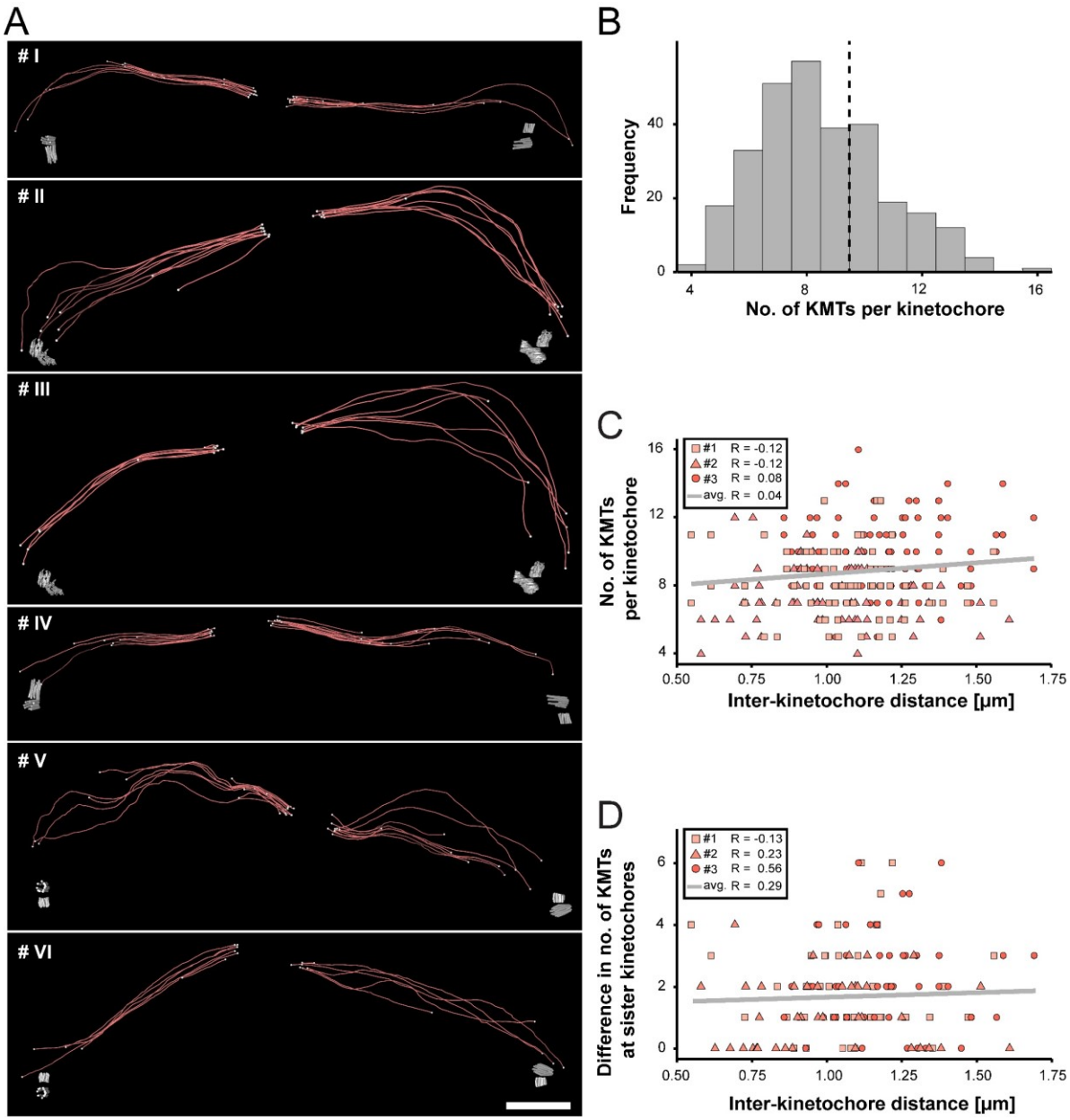

Figure 3. Number of KMTs attached per kinetochore

(**A**) Example models of individual sister k-fibers extracted from the full 3D reconstructions of metaphase spindles. KMTs are shown as red lines. The ends of the KMTs are indicated by white spheres. The centrioles (grey) are also shown. Scale bar, 1.5 µm. (**B**) Histogram plot showing the frequency with which a given number of KMTs per kinetochore was detected. This plot includes data from all three spindle reconstructions. (**C**) Correlation of the inter-kinetochore distance and the number of KMTs associated per kinetochore. The Pearson's correlation coefficient for each data set and the average for all data sets are given. (**D**) Correlation of the inter-kinetochore distance and the difference (delta) in the number of KMTs

bioRxiv preprint doi: https://doi.org/10.1101/2021.11.13.468347; this version posted November 13, 2021. The copyright holder for this preprint (which was not certified by peer review) is the author/funder. All rights reserved. No reuse allowed without permission.

associated with respective sister kinetochores. The Pearson's correlation coefficient for each data set and the average for all data sets are given.

bioRxiv preprint doi: https://doi.org/10.1101/2021.11.13.468347; this version posted November 13, 2021. The copyright holder for this preprint (which was not certified by peer review) is the author/funder. All rights reserved. No reuse allowed without permission.

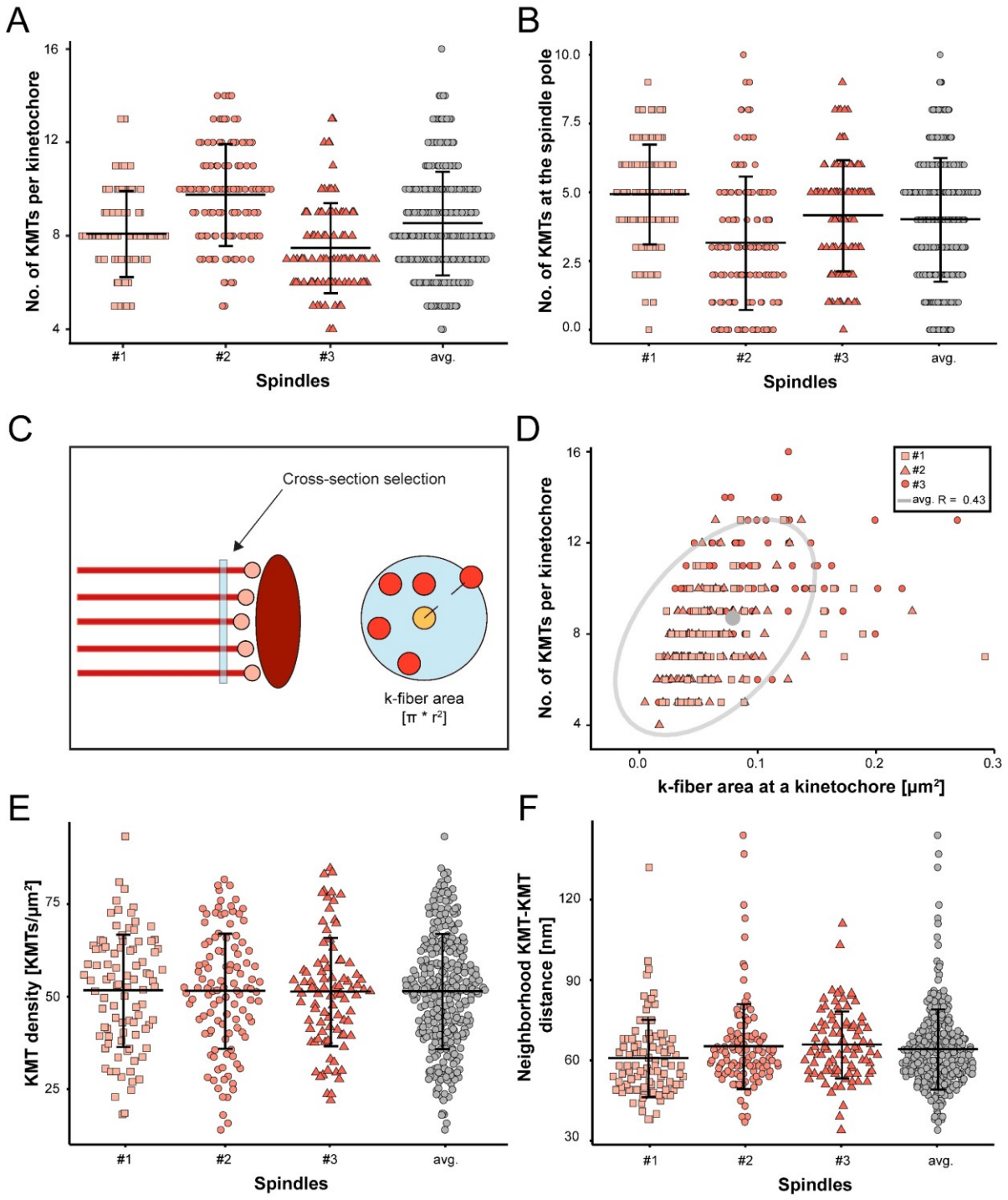

Figure 3-figure supplement 1. Correlation of k-fiber circumference and number of attached KMTs

(**A**) Graph showing the number of KMTs per kinetochore for each data set and the average number for all data sets (mean ± STD). (**B**) Plot showing the distribution of KMT minus ends in k-fibers for each data set and the average number for all data sets (mean ± STD). (**C**) Schematic illustration of the analysis of k-fiber area for indirect measurement of the

bioRxiv preprint doi: https://doi.org/10.1101/2021.11.13.468347; this version posted November 13, 2021. The copyright holder for this preprint (which was not certified by peer review) is the author/funder. All rights reserved. No reuse allowed without permission.

kinetochore area. MTs (red lines) with their ends (spheres in light red) and the kinetochore (ellipsoid in dark red) are shown. The measurement of the cross-section of a k-fiber in the vicinity of the KMT ends is indicated by a blue bar (left). The k-fiber area is given by a circle (blue) enclosing all KMTs (circle reaching to the middle of the peripheral KMTs). (**D**) Correlation of k-fiber area and number of KMTs per kinetochore for all reconstructed spindles. The grey ellipse indicates a 95% confidence interval for all data and the grey dot indicates the average kinetochore area. (**E**) Graph showing the density of KMTs at the kinetochore (KMTs/μm^2) for each 3D reconstruction and all data sets (mean ± STD). (**F**) Plot showing the neighborhood KMT-KMT distance at the kinetochore for the individual data sets (mean ± STD); The average number for all data sets is also given.

bioRxiv preprint doi: https://doi.org/10.1101/2021.11.13.468347; this version posted November 13, 2021. The copyright holder for this preprint (which was not certified by peer review) is the author/funder. All rights reserved. No reuse allowed without permission.

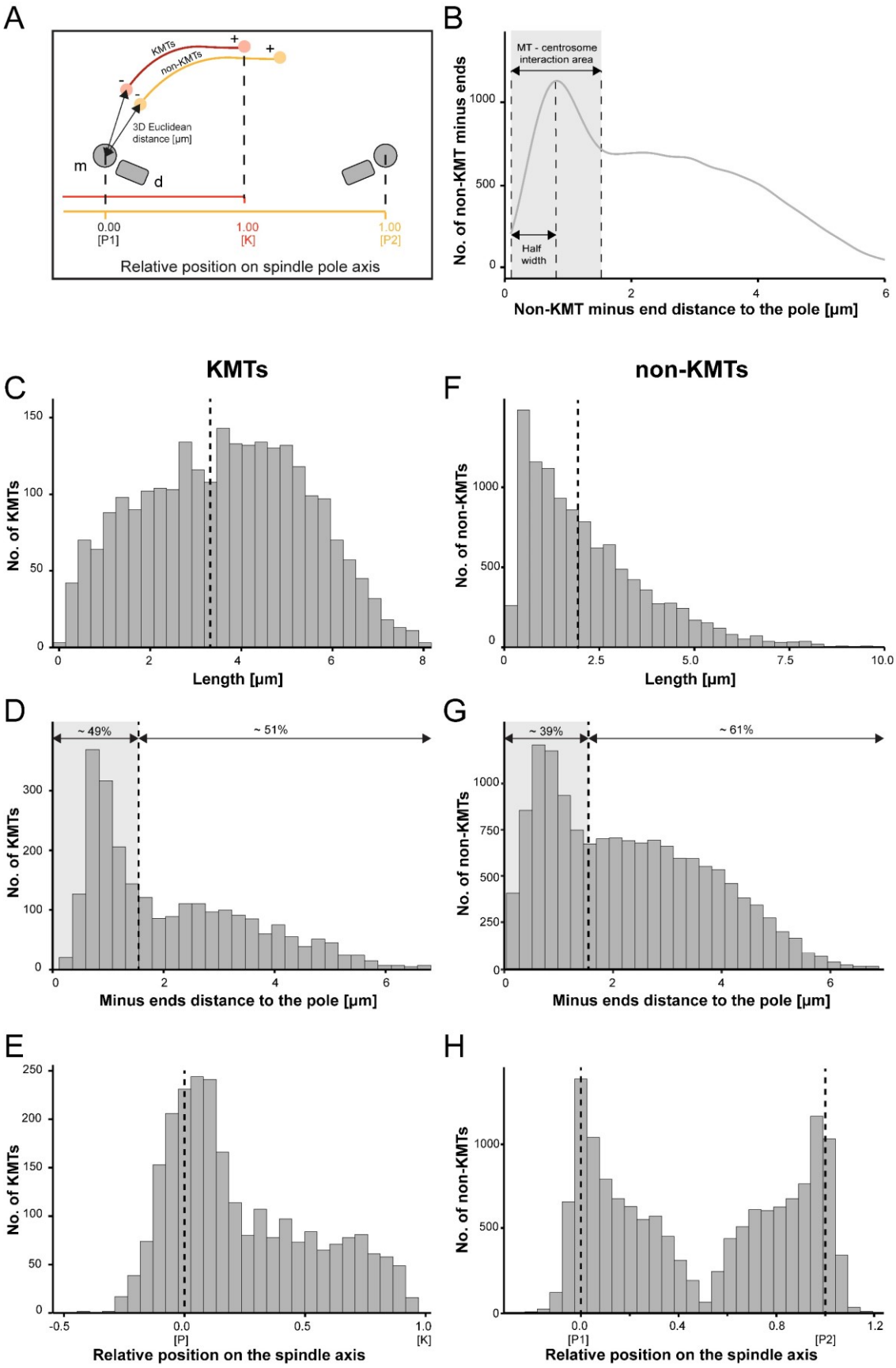

900

bioRxiv preprint doi: https://doi.org/10.1101/2021.11.13.468347; this version posted November 13, 2021. The copyright holder for this preprint (which was not certified by peer review) is the author/funder. All rights reserved. No reuse allowed without permission.

Figure 4. Length distribution and minus end positioning of MTs in metaphase spindles

(**A**) Schematic illustration of MT minus end positioning along the spindle axis (P1 - pole1; P2 - pole2; K - kinetochore). A KMT (red line) with its ends (red spheres) and a non-KMT (yellow line) with its ends (yellow spheres) are shown. The 3D Euclidean distance of both the KMT and the non-KMT minus end to the center of the mother centriole can be calculated. The relative position of the KMT minus ends along the pole-to-kinetochore axis and the non-KMT minus ends along the pole-to-pole axis was also determined. (**B**) Calculation of the interaction area of MTs with the centrosomes. Graph showing the number of non-KMT minus ends plotted against their distance to the pole (i.e. to the center of the mother centriole). The determined area of the interaction of non-KMTs with the centrosome and the half-width of this area is indicated in grey. (**C**) Histogram showing the length distribution of KMTs from all data sets. The dashed line indicates the average length of KMTs. (**D**) Histogram showing the distribution of the KMT minus end distances to the center of the mother centriole. The area of interaction of MTs with the centrosome is defined as in B and indicated by a grey area (dashed line shows the border of this area). (**E**) Histogram showing the relative position of the KMT minus ends on the spindle axis. The positions of the spindle pole (P=0, dashed line) and the kinetochore (K=1) are indicated. (**F**) Histogram showing the length distribution of non-KMTs. The dashed line indicates the average length of non-KMTs. (**G**) Histogram showing the distribution of the non-KMT minus end distances to the center of the mother centriole. (**H**) Plot showing the relative position of the non-KMT minus ends on the spindle axis. The positions of the spindle poles (P1=0, P2=1) are indicated.

bioRxiv preprint doi: https://doi.org/10.1101/2021.11.13.468347; this version posted November 13, 2021. The copyright holder for this preprint (which was not certified by peer review) is the author/funder. All rights reserved. No reuse allowed without permission.

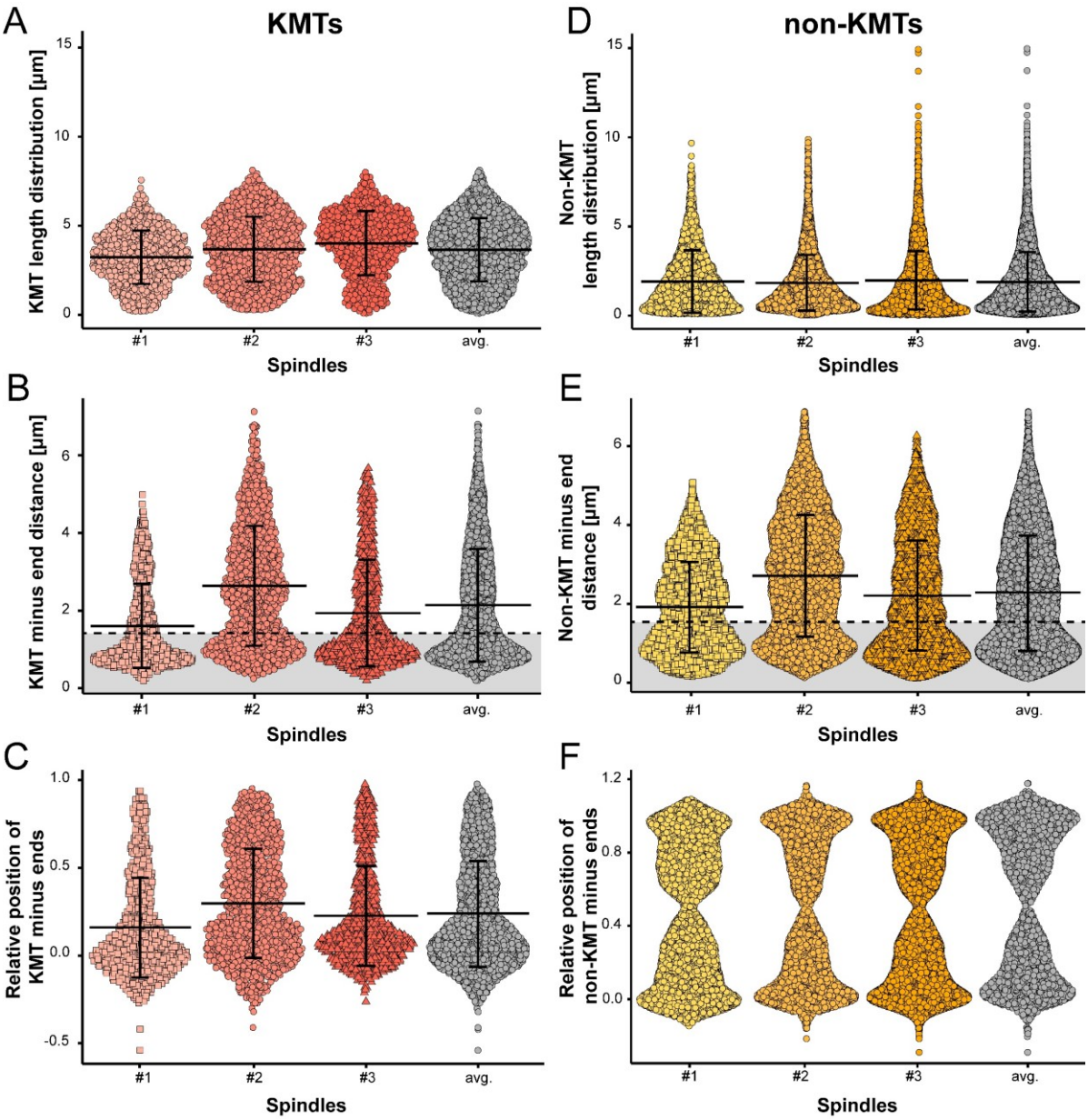

Figure 4-figure supplement 1. KMT length and minus-end distribution

(**A**) Beeswarm plot showing the length distribution of KMTs in all data sets and the average values. (**B**) Plot showing the distribution of KMT minus end distances to the center of the mother centriole. The area of interaction of the MT ends with the centrosomes is indicated in grey (with a dashed line showing the border of this area). (**C**) Plot showing the relative position of KMT minus ends on the spindle axis (P=0, K=1). (**D**) Length distribution of non-KMTs. (**E**) Distribution of the distances of the non-KMT minus ends to the center of the mother centriole. (**F**) The relative position of non-KMT minus ends on the pole (P1)-to-pole (P2) axis.

bioRxiv preprint doi: https://doi.org/10.1101/2021.11.13.468347; this version posted November 13, 2021. The copyright holder for this preprint (which was not certified by peer review) is the author/funder. All rights reserved. No reuse allowed without permission.

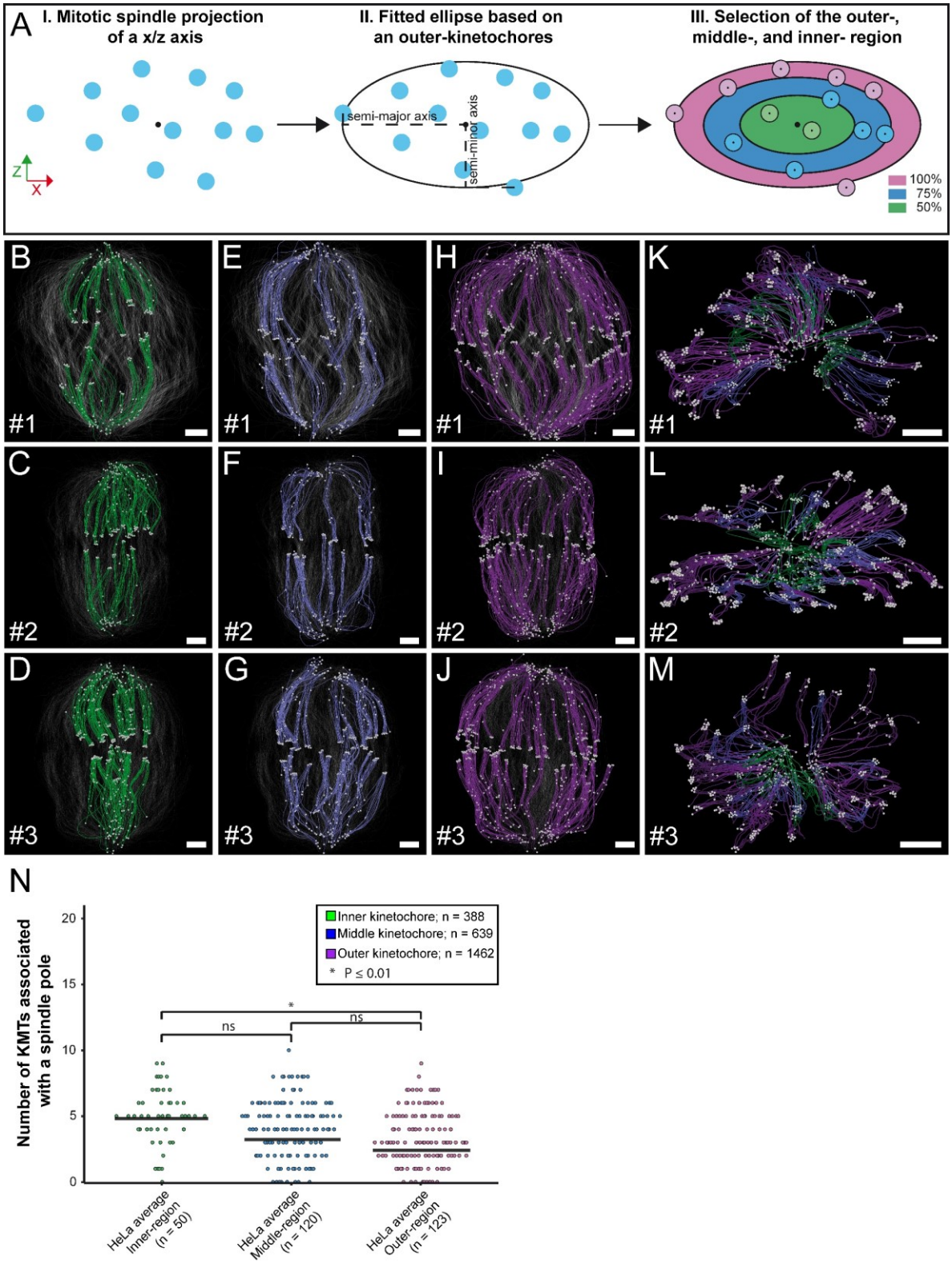

932

933 **Figure 4-figure supplement 2. Correlation of KMT length and minus-end**
934 **distribution with positioning on the metaphase plate**

935 (**A**) Schematic illustration of the selection of kinetochores and the corresponding k-fiber
936 positions on the x/z projection of the metaphase plate. Kinetochores are indicated as blue

bioRxiv preprint doi: https://doi.org/10.1101/2021.11.13.468347; this version posted November 13, 2021. The copyright holder for this preprint (which was not certified by peer review) is the author/funder. All rights reserved. No reuse allowed without permission.

circles. The semi-minor and the semi-major axis indicate the axis of a fitted ellipse into all kinetochores. The ellipse is divided into three parts representing the percentage of occupancy of the ellipse (0-50%, inner-kinetochores, green; 50-75%, middle-kinetochores, blue; and 75-100%, outer-kinetochores, purple). (**B-D**) Perspective view on a metaphase spindle with selected inner-kinetochores. (**E-G**) Perspective view with selected middle-kinetochores. (**H-J**) Perspective view with selected outer-kinetochores. (**K-M**) Perspective view on a cross-section of the spindle with all defined k-fiber classes. (**N**) Plot showing the number of KMT minus ends in each k-fiber associated with the spindle pole for three positional regions in the mitotic spindle for all data sets. The mean of the KMT minus-end number is indicated.

bioRxiv preprint doi: https://doi.org/10.1101/2021.11.13.468347; this version posted November 13, 2021. The copyright holder for this preprint (which was not certified by peer review) is the author/funder. All rights reserved. No reuse allowed without permission.

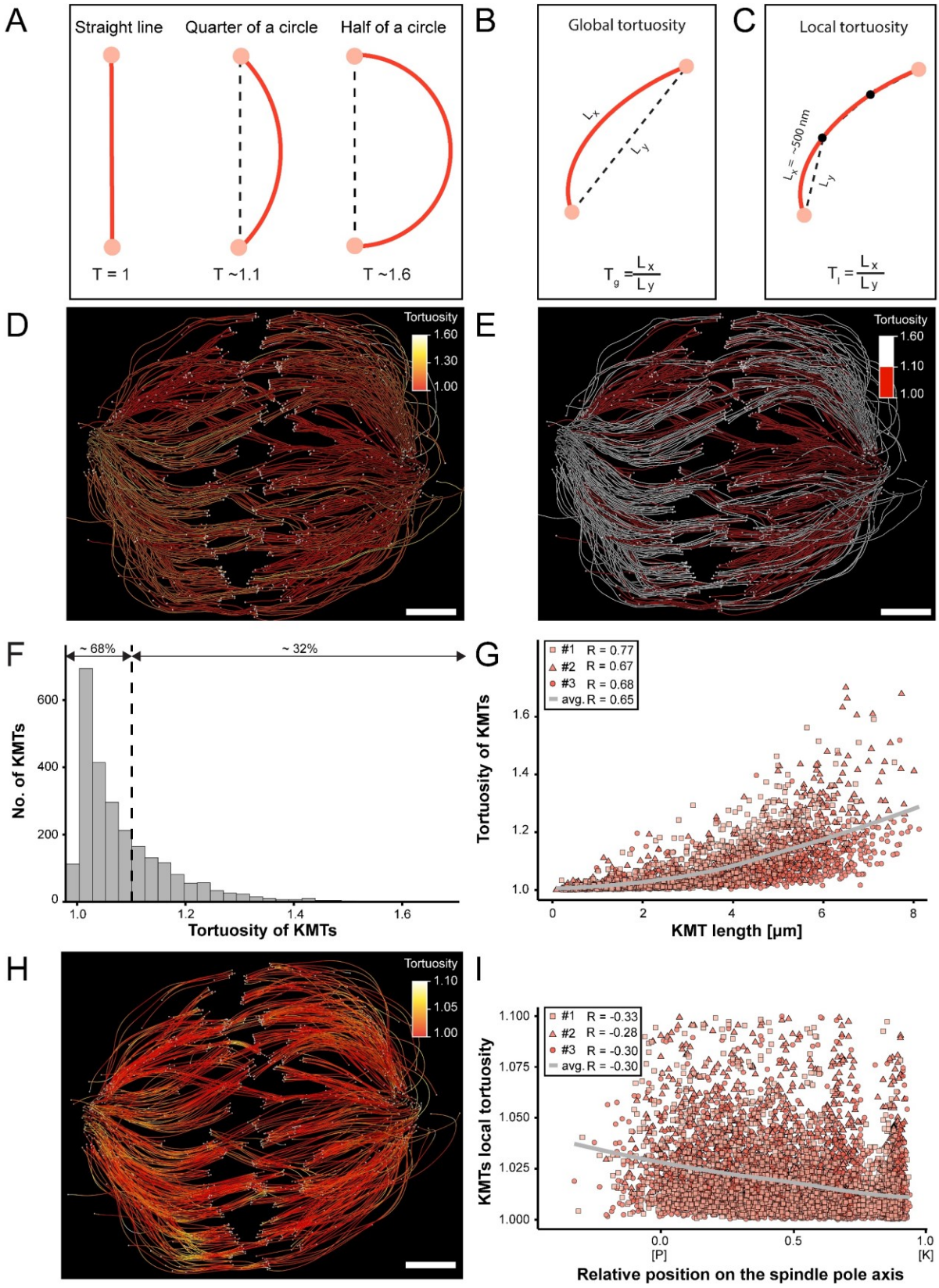

946

bioRxiv preprint doi: https://doi.org/10.1101/2021.11.13.468347; this version posted November 13, 2021. The copyright holder for this preprint (which was not certified by peer review) is the author/funder. All rights reserved. No reuse allowed without permission.

Figure 5. Global and local tortuosity of KMTs

(**A**) Schematic illustration of tortuosity (T) as given for a straight line, and a quarter and a half of a circle. (**B**) Schematic illustration of global tortuosity (T_g) of KMTs given by the ratio of the spline length (L_x) to the 3D Euclidean distance between the KMT ends (L_y). (**C**) Schematic illustration of KMT local tortuosity (T_l) as given by division segments with a length of 500 nm. (**D**) Three-dimensional model of k-fibers (spindle #1) showing the global tortuosity of KMTs as indicated by color coding (top left corner). (**E**) Perspective view as shown in C. Straight KMTs (tortuosity of 1.0 - 1.1, red) and curved KMTs (tortuosity ≥ 1.1, white) are highlighted. (**F**) Histogram showing the frequency of different degrees of KMT tortuosity. A tortuosity of 1.1 is indicated by a dashed line. (**G**) Correlation of the global tortuosity and the length of KMTs. The Pearson's correlation coefficient is given for each reconstructed spindle. The grey line indicates the local regression calculated by the loess method. (**H**) Three-dimensional model of k-fibers (spindle #1) showing the local tortuosity of KMTs as indicated by color-coding. (**I**) Correlation of the local tortuosity of KMTs with the relative position along the pole (P)-to-kinetochore (K) distance. Scale bars, 1 µm.

bioRxiv preprint doi: https://doi.org/10.1101/2021.11.13.468347; this version posted November 13, 2021. The copyright holder for this preprint (which was not certified by peer review) is the author/funder. All rights reserved. No reuse allowed without permission.

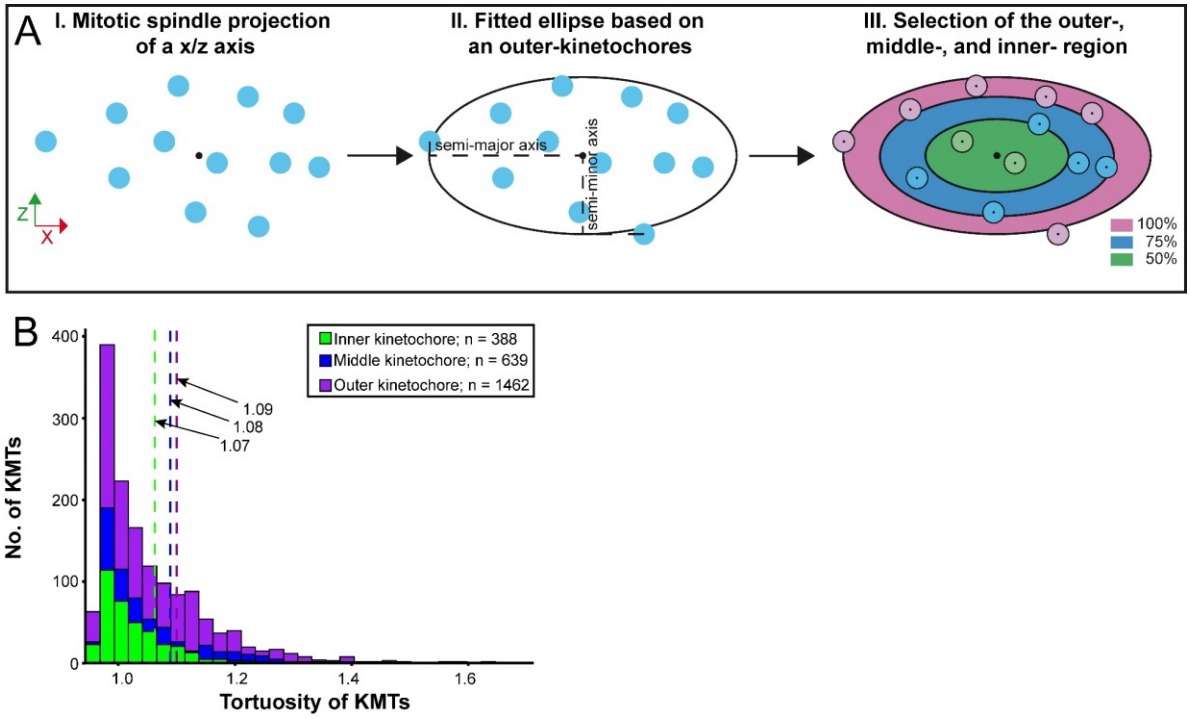

963

964 **Figure 5-figure supplement 1. Correlation of MT tortuosity with k-fiber**
965 **positioning in the spindle**

966 (**A**) Selection of kinetochore and corresponding k-fiber positions on the x/z projection of the
967 metaphase plate. Kinetochores are indicated as blue circles. The semi-minor and the semi-
968 major axis indicate the axis of a fitted ellipse into all kinetochores. The ellipse is divided into
969 three parts representing the percentage of occupancy of the ellipse (0-50%, inner-
970 kinetochores, green; 50-75%, middle-kinetochores, blue; and 75-100%, outer-kinetochores,
971 purple). (**B**) Histogram showing the frequency of different degrees of KMT tortuosity in relation
972 to k-fiber position in the mitotic spindle. The mean tortuosity of each position class is indicated.

bioRxiv preprint doi: https://doi.org/10.1101/2021.11.13.468347; this version posted November 13, 2021. The copyright holder for this preprint (which was not certified by peer review) is the author/funder. All rights reserved. No reuse allowed without permission.

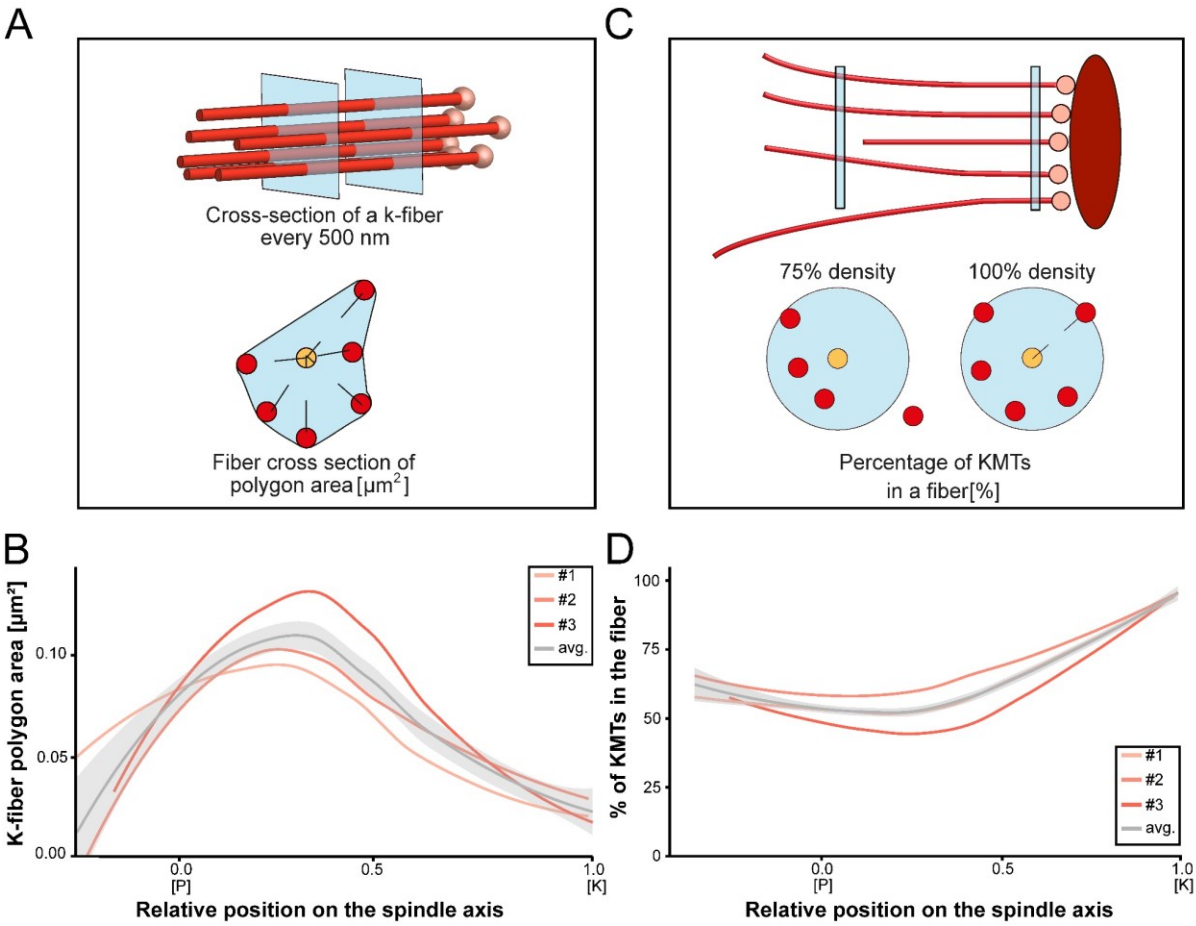

Figure 6. Shape of k-fibers

(**A**) Schematic illustration of the polygon area-analysis of k-fiber cross-sections. KMTs are shown in red, KMT ends as red spheres. The cross-section of the given k-fiber is shown as a blue square and the median position of all KMTs in the cross-section as a yellow circle. (**B**) Correlation of the k-fiber polygon area and the relative position on the pole [P]-to-kinetochore [K] axis. (**C**) Schematic illustration of the k-fiber density analysis. For each k-fiber, a radius at the kinetochore was estimated by calculating a minimum circle enclosing all KMTs. The determined radius was then enlarged by factor 2 to account for k-fiber flexibility. Along with the k-fiber, the number of KMTs enclosed in the selected radius was then measured. (**D**) Correlation of the KMT density and the relative position along pole [P]-to-kinetochore [K] axis. For each reconstructed spindle, data sets are presented as polynomial lines showing local regression calculated with the loess method. Average values with standard deviations are shown in grey.

bioRxiv preprint doi: https://doi.org/10.1101/2021.11.13.468347; this version posted November 13, 2021. The copyright holder for this preprint (which was not certified by peer review) is the author/funder. All rights reserved. No reuse allowed without permission.

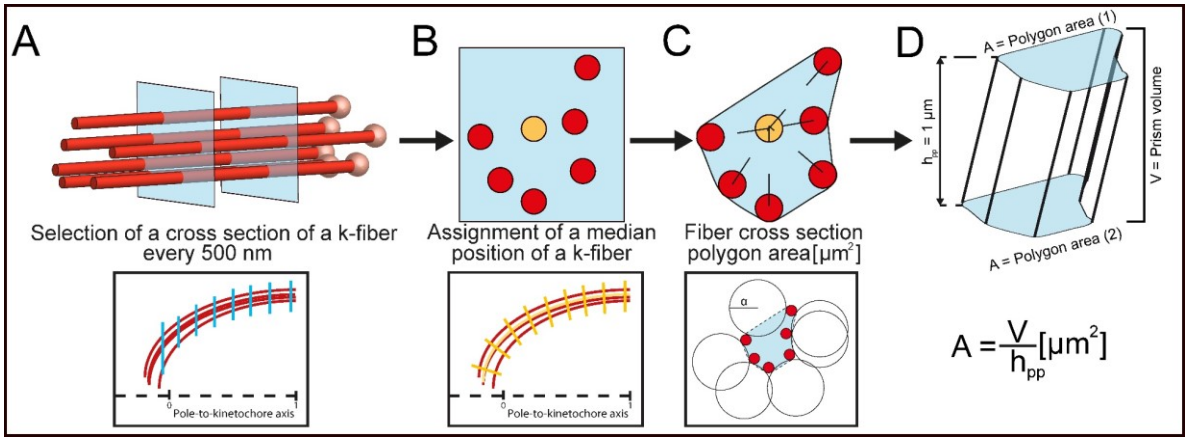

Figure 6-figure supplement 1. Schematic illustration of the analysis of k-fiber area and density

(**A**) Selection of cross-sections on a k-fiber (KMTs in red, KMT ends, red spheres) every 500 nm (upper row - blue squares; lower row - blue lines). (**B**) Assignment of a median position (upper row - yellow circle) for each cross-section and geometric correction of each cross-section based on the k-fiber's curvature (lower row - yellow lines). (**C**) Calculation of the polygon area (upper row). The polygon area was calculated using the alpha shape algorithm. For each cross-section, circles with diameter defined by α (lower row - black lines) were fitted around the 2D projection of KMTs. Polygon shape was created by drawing lines around KMTs that were at the junction of fitted circles (lower row - black dashed lines). (**D**) Calculation of the polygon area from the created prism shape. For this, a polygon area was duplicated and moved in XYZ Euclidean space by 1 μm to create a prism shape. The polygon area (A) is given by dividing a prism volume [μm^2] by a prism high (h_{pp} = 1 μm).

bioRxiv preprint doi: https://doi.org/10.1101/2021.11.13.468347; this version posted November 13, 2021. The copyright holder for this preprint (which was not certified by peer review) is the author/funder. All rights reserved. No reuse allowed without permission.

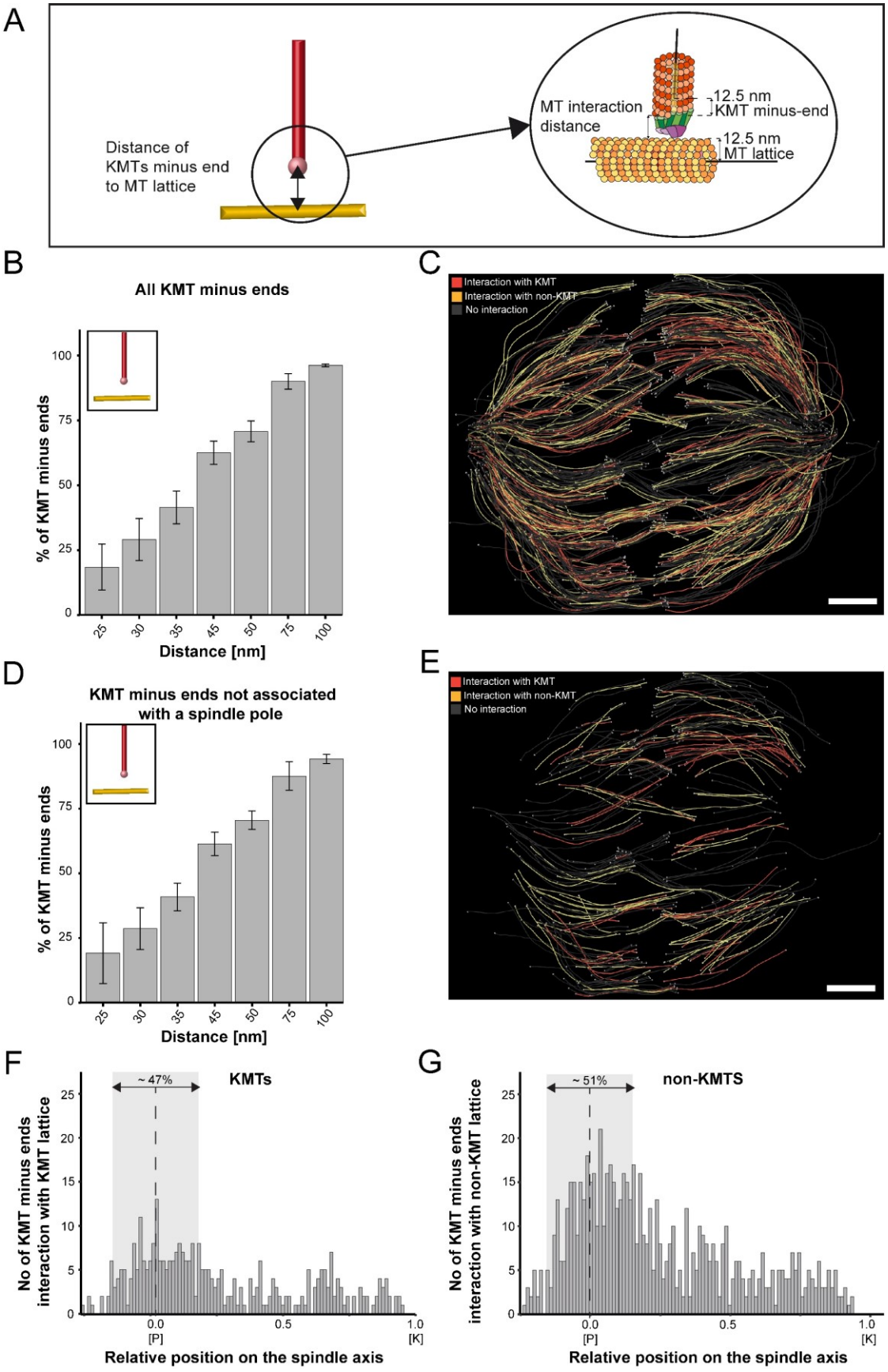

1001

bioRxiv preprint doi: https://doi.org/10.1101/2021.11.13.468347; this version posted November 13, 2021. The copyright holder for this preprint (which was not certified by peer review) is the author/funder. All rights reserved. No reuse allowed without permission.

Figure 7. Association of KMT minus ends with the MT network

(**A**) Schematic illustration of the association of KMT minus ends with MT lattices showing a KMT (red line) with its minus end (red sphere) located close to the lattice of a non-KMT (yellow line). The distance from a KMT minus end to the center of a non-KMT lattice is estimated. (**B**) Bar plot showing the percentage of all KMT minus ends associated with a MT lattice depending on defined distances of association (25 - 100 nm). The standard deviations are given. (**C**) A three-dimensional model showing the interaction pattern of all KMT minus ends associated with MTs based on an interaction distance of 35 nm (data obtained from spindle #1). KMTs with their minus end associated with other KMTs are labeled in red, KMTs with an association to non-KMTs are marked in yellow. KMTs without any association to other MTs are shown in grey. (**D**) Bar plot showing the percentage of KMT minus ends not associated with the centrosome interaction area. The association with MT lattices is shown in relation to the chosen distance of association. (**E**) Three-dimensional model of KMTs with their minus ends not attached to the centrosome and associated with MT lattices. Colors are shown as displayed in C. (**F**) Graph showing the number of KMT minus ends interacting with KMT lattices within a distance of 35 nm. The number of KMT minus ends is plotted against the relative position on the spindle axis (P, pole; K, kinetochore). (**G**) Bar plot showing the number of KMT minus ends interacting with non-KMT lattices within a distance of 35 nm. The graph gives the relative position of the non-KMT minus ends plotted against the relative position on the pole axis. Data from the three reconstructed spindles are shown. Scale bars, 1 µm

bioRxiv preprint doi: https://doi.org/10.1101/2021.11.13.468347; this version posted November 13, 2021. The copyright holder for this preprint (which was not certified by peer review) is the author/funder. All rights reserved. No reuse allowed without permission.

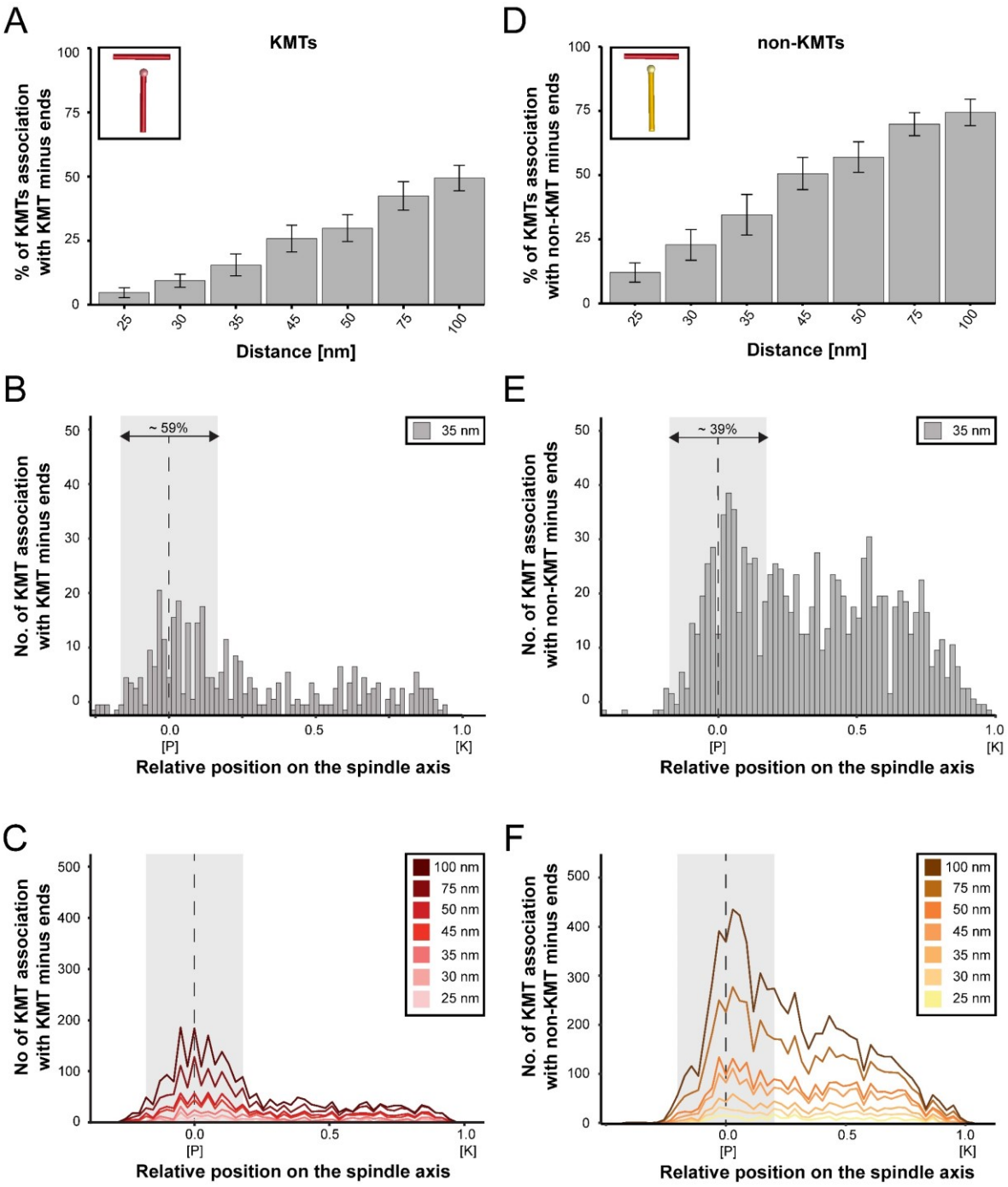

Figure 7-figure supplement 1. Association of KMT lattices with MT minus ends

(**A**) Bar plot showing the percentage of KMT lattices associated with other KMT minus ends depending on defined interaction distances. The standard deviations are indicated. (**B**) Graph showing the number of KMT lattices associated with other KMT minus ends plotted along with the relative position on the spindle axis (P, pole; K, kinetochore). The distance of MT interaction is 35 nm. The percentage of KMT association at the MT-centrosome interaction

bioRxiv preprint doi: https://doi.org/10.1101/2021.11.13.468347; this version posted November 13, 2021. The copyright holder for this preprint (which was not certified by peer review) is the author/funder. All rights reserved. No reuse allowed without permission.

area is indicated. (**C**) Plot showing the number of KMT lattices associated with KMT minus ends as shown in B. The plot shows the number of associations for distances of 25, 30, 35, 45, 50, 75 and 100 nm. (**D**) Bar plot showing the percentage of KMT lattices associated with non-KMT minus ends. The distance of MT interaction is 35 nm. (**E**) Line plot showing the number of KMT lattices associated with other non-KMT minus ends plotted against the relative position on the spindle axis. The percentage of KMT association at the MT-centrosome interaction area is indicated. All graphs show mean values from the three reconstructed spindles. (**F**) Plot showing the number of non-KMT lattices associated with KMT minus ends as shown in E. The plot shows the number of associations for distances of 25, 30, 35, 45, 50, 75 and 100 nm.

bioRxiv preprint doi: https://doi.org/10.1101/2021.11.13.468347; this version posted November 13, 2021. The copyright holder for this preprint (which was not certified by peer review) is the author/funder. All rights reserved. No reuse allowed without permission.

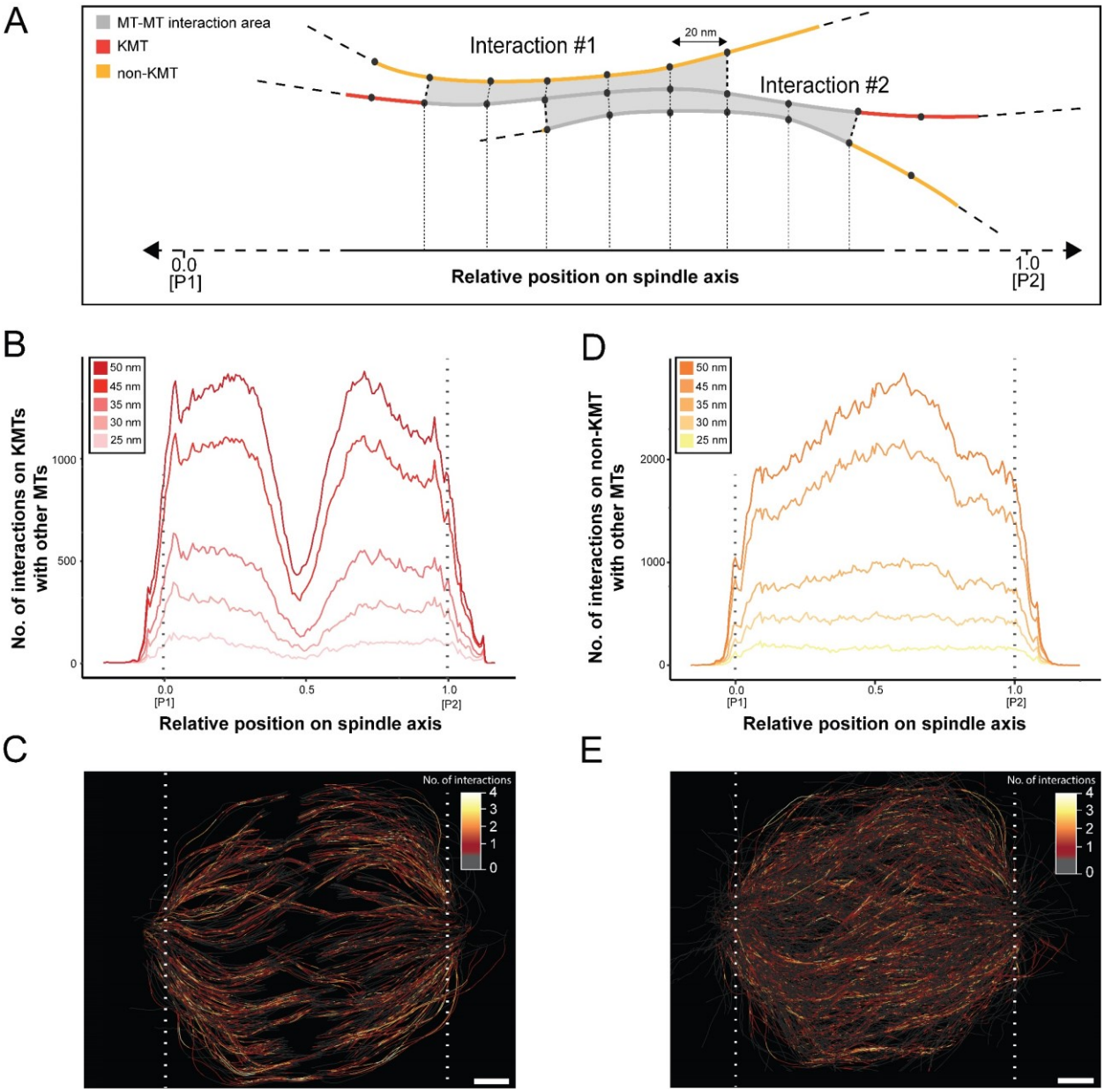

Figure 8. Positions of MT-MT associations

(**A**) Schematic illustration of MT-MT associations. The interactions are given in intervals of 20 nm. This allows mapping of the number of interactions on the spindle pole axis. KMTs are illustrated in red, non-KMTs in yellow, areas of MT-MT association in grey. (**B**) Plot showing number of KMTs associated with other MTs plotted against the relative position of the association on a spindle axis. (**C**) 3D model of all KMTs showing regions of MT-MT association within a distance of 35 nm or closer. Each KMT segment is color-coded according to the number of associations. (**D**) The number of non-KMTs associated with neighboring MTs plotted against the relative position of the association on a spindle axis. Plots are shown for

bioRxiv preprint doi: https://doi.org/10.1101/2021.11.13.468347; this version posted November 13, 2021. The copyright holder for this preprint (which was not certified by peer review) is the author/funder. All rights reserved. No reuse allowed without permission.

five different thresholds of MT-MT association distances. (**E**) 3D model of all non-KMTs showing regions of MT-MT association within a distance of 35 nm or closer. Scale bars, 1 µm.

bioRxiv preprint doi: https://doi.org/10.1101/2021.11.13.468347; this version posted November 13, 2021. The copyright holder for this preprint (which was not certified by peer review) is the author/funder. All rights reserved. No reuse allowed without permission.

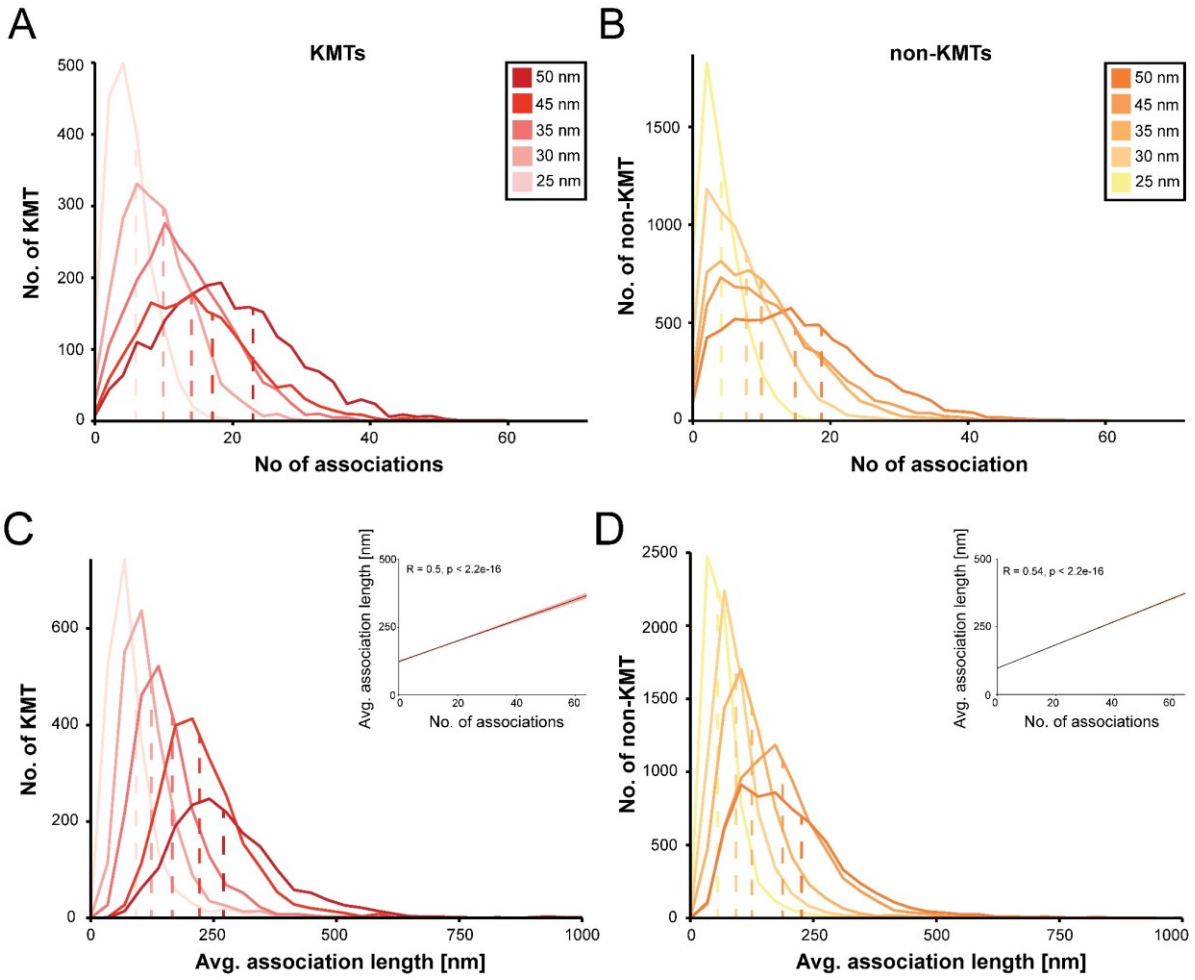

Figure 8-figure supplement 1. Association of KMT lattices with MT minus ends

(**A**) Number of KMTs plotted against the number of associations with other MTs in the spindle per individual KMT. Plots are shown for five different distances between MT-MTs. (**B**) Number of KMTs plotted against the average length of MT-MT association per individual KMT. (**C**) The number of non-KMTs plotted against the number of associations. Plots are shown for five different thresholds of MT-MT association distances. (**D**) The number of non-KMTs plotted against the average length of MT-MT association *per* individual non-KMT. A correlation plot is also shown for the number of MT associations and length for KMTs and non-KMTs.

bioRxiv preprint doi: https://doi.org/10.1101/2021.11.13.468347; this version posted November 13, 2021. The copyright holder for this preprint (which was not certified by peer review) is the author/funder. All rights reserved. No reuse allowed without permission.

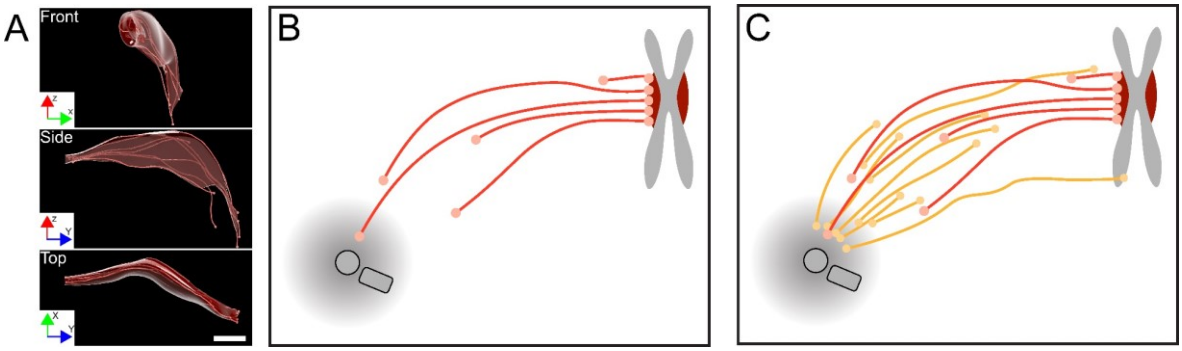

Figure 9. Model of a k-fiber showing a semi-direct connection between a kinetochore and spindle poles

(**A**) Three-dimensional model of a selected k-fiber with an overlay k-fiber area drawn around KMTs using the alpha shape method. The same k-fiber is shown from three different perspectives (front, side and top view). (**B**) Schematic model of a semi-direct connection between a kinetochore (chromosome in grey with paired kinetochores in dark red) and a spindle pole (with centered centrioles) as established for a single k-fiber. KMTs are shown in red. MT ends are indicated as spheres. (**C**) Schematic model of the k-fiber interaction with a non-KMTs network. KMTs are shown in red, non-KMTS in yellow, chromosomes with paired kinetochores in dark red and a spindle pole with centrioles in grey. MTs ends are indicated as spheres. Scale bar, 1 µm.

bioRxiv preprint doi: https://doi.org/10.1101/2021.11.13.468347; this version posted November 13, 2021. The copyright holder for this preprint (which was not certified by peer review) is the author/funder. All rights reserved. No reuse allowed without permission.

Movie Supplements

Figure 2-movie supplement 1. Generation of a 3D model from joined serial electron tomograms displaying spindle #1

This video shows a series of stitched 3D reconstructions of spindle #1 and the corresponding 3D model. The stacking of serial tomograms to increase the tomographic volume is illustrated. The MTs are shown in white lines, chromosomes are illustrated in blue. This movie corresponds to Figure 2C.

Figure 2-movie supplement 2. Generation of a 3D model from joined serial electron tomograms displaying spindle #2

This video shows a series of stitched 3D reconstructions of spindle #2 and the corresponding 3D model. The stacking of serial tomograms to increase the tomographic volume is illustrated. The MTs are shown in white lines, chromosomes are illustrated in blue. This movie corresponds to Figure 2D.

Figure 2-movie supplement 3. Generation of a 3D model from joined serial electron tomograms displaying spindle #3

This video shows a series of stitched 3D reconstructions of spindle #3 and the corresponding 3D model. The stacking of serial tomograms to increase the tomographic volume is illustrated. The MTs are shown in white lines, chromosomes are illustrated in blue. This movie corresponds to Figure 2E.

Figure 2-movie supplement 4. Movie showing an overview of KMTs in spindle #1

This video shows a 3D model of the reconstructed metaphase spindle #1. Non-KMTs are shown in yellow, the KMTs are shown in red, chromosomes are illustrated in blue and centrioles in grey. This movie corresponds to Figure 2F.

bioRxiv preprint doi: https://doi.org/10.1101/2021.11.13.468347; this version posted November 13, 2021. The copyright holder for this preprint (which was not certified by peer review) is the author/funder. All rights reserved. No reuse allowed without permission.

Figure 2-movie supplement 5. Movie showing an overview of KMTs in spindle #2

This video shows a 3D model of the reconstructed metaphase spindle #1. Non-KMTs are shown in yellow, the KMTs are shown in red, chromosomes are illustrated in blue and centrioles in grey. This movie corresponds to Figure 2G.

Figure 2-movie supplement 6. Movie showing an overview of KMTs in spindle #3

This video shows a 3D model of the reconstructed metaphase spindle #1. Non-KMTs are shown in yellow, the KMTs are shown in red, chromosomes are illustrated in blue and centrioles in grey. This movie corresponds to Figure 2H.

Figure 3-movie supplement 1. Movie of the 3D reconstruction of a single k-fiber

This video shows a 3D model of the selected sister k-fibers of spindle #1. The KMTs are shown in red, the KMT ends by white spheres, the centrioles in grey. This movie corresponds to Figure 3A (# I).

Figure 3-movie supplement 2. Movie of the 3D reconstruction of a single k-fiber

This video shows a 3D model of the selected sister k-fibers of spindle #1. The KMTs are shown in red, the KMT ends by white spheres, the centrioles in grey. This movie corresponds to Figure 3A (# II).

Figure 3-movie supplement 3. Movie of the 3D reconstruction of a single k-fiber

This video shows a 3D model of the selected sister k-fibers of spindle #1. The KMTs are shown in red, the KMT ends by white spheres, the centrioles in grey. This movie corresponds to Figure 3A (# III).

bioRxiv preprint doi: https://doi.org/10.1101/2021.11.13.468347; this version posted November 13, 2021. The copyright holder for this preprint (which was not certified by peer review) is the author/funder. All rights reserved. No reuse allowed without permission.

Figure 3-movie supplement 4. Movie of the 3D reconstruction of a single k-fiber

This video shows a 3D model of the selected sister k-fibers of spindle #1. The KMTs are shown in red, the KMT ends by white spheres, the centrioles in grey. This movie corresponds to Figure 3A (# IV).

Figure 3-movie supplement 5. Movie of the 3D reconstruction of a single k-fiber

This video shows a 3D model of the selected sister k-fibers of spindle #1. The KMTs are shown in red, the KMT ends by white spheres, the centrioles in grey. This movie corresponds to Figure 3A (# V).

Figure 3-movie supplement 6. Movie of the 3D reconstruction of a single k-fiber

This video shows a 3D model of the selected sister k-fibers of spindle #1. The KMTs are shown in red, the KMT ends by white spheres, the centrioles in grey. This movie corresponds to Figure 3A (# VI).

Figure 5-movie supplement 1. Movie showing the analysis of k-fiber tortuosity in spindle #1

This video shows a 3D model of all KMTs with indicated global tortuosity of spindle #1. KMTs are shown in color coding as indicated in Figure 5C. KMT ends are shown as white spheres, centrioles in grey. This movie corresponds to Figure 5C.

Figure 5-movie supplement 2. Movie showing the analysis of k-fiber tortuosity in spindle #2

This video shows a 3D model of all KMTs with indicated global tortuosity of spindle #1. KMTs are shown in color coding as indicated in Figure 5C. KMT ends are shown as white spheres, centrioles in grey. This movie corresponds to Figure 5C (example of spindle #2 shown as a movie only).

bioRxiv preprint doi: https://doi.org/10.1101/2021.11.13.468347; this version posted November 13, 2021. The copyright holder for this preprint (which was not certified by peer review) is the author/funder. All rights reserved. No reuse allowed without permission.

Figure 5-movie supplement 3. Movie showing the analysis of k-fiber tortuosity in spindle #3

This video shows a 3D model of all KMTs with indicated global tortuosity of spindle #1. KMTs are shown in color coding as indicated in Figure 5C. KMT ends are shown as white spheres, centrioles in grey. This movie corresponds to Figure 5C (example of spindle #3 shown as a movie only).

Figure 7-movie supplement 1. Movie showing associations of KMT minus ends with MT lattices in spindle #1

This video shows a 3D model of all KMTs from spindle #1. KMT minus ends interacting with other MTs with association distances ranging from 25 to 100 nm are shown. KMT minus ends interacting with either KMT or non-KMT lattices are indicated in red or yellow, respectively. KMTs without any interactions are shown in grey. This movie corresponds to Figure 7C.

Figure 8-movie supplement 1. Movie showing associations of KMT lattices with neighbor MTs

This video shows a 3D model of all KMTs in spindle #1. KMT lattices interacting with other MT lattices within MT distances ranging from 25 to 50 nm are shown. KMTs are shown as grey lines with color-coded regions showing the number of MT-MT associations. This movie corresponds to Figure 8C.

Figure 8-movie supplement 2. Movie showing associations of non-KMTs with neighbor MTs

This video shows a 3D model of all non-KMTs showing regions of MT-MT associations in spindle #1 over increasing MT distances ranging from 25 to 50 nm. Non-KMTs are shown as grey lines with color-coded regions showing the number of MT-MT associations. This movie corresponds to Figure 8E.

bioRxiv preprint doi: https://doi.org/10.1101/2021.11.13.468347; this version posted November 13, 2021. The copyright holder for this preprint (which was not certified by peer review) is the author/funder. All rights reserved. No reuse allowed without permission.

Tables

Table 1. Characterization of the 3D-reconstructed metaphase spindles in HeLa cells

Data set / Analysis	Spindle pole distance [µm]	Inter-kinetochore distance [µm]	Total no. of MTs	No. of kinetochores	No. of KMTs	No. of non-KMTs	No. of k-fibers
Spindle #1	7.16	1.07 ± 0.20 (n=43)	4884	92	797 (16.3%)	4087 (83.7%)	92
Spindle #2	10.39	1.21 ± 0.21 (n=50)	8047	110	1102 (13.7%)	6945 (86.3%)	110
Spindle #3	9.48	1.02 ± 0.29 (n=40)	5904	90	680 (11.5%)	5224 (88.5%)	90

bioRxiv preprint doi: https://doi.org/10.1101/2021.11.13.468347; this version posted November 13, 2021. The copyright holder for this preprint (which was not certified by peer review) is the author/funder. All rights reserved. No reuse allowed without permission.

1177 **Table 2. Quantitative analysis of KMTs and non-KMTs**

Data set / Analysis	Length of KMTs [µm]	Length of non-KMTs [µm]	No. of KMTs per kinetochore	No. of KMTs at centrosome interaction area	Mean KMT minus end distance to poles [µm]	No. of KMTs associated with poles [%]	No. of non-KMTs associated with poles [%]
Spindle #1	3.23 (±1.49)	2.03 (±1.6)	8.04 (±1.86)	4.1 (±1.8)	1.16	62.2	44.5
Spindle #2	3.69 (±1.87)	1.85 (±1.55)	9.75 (±2.18)	2.4 (±2.0)	2.47	53.6	28.8
Spindle #3	4.03 (±1.79)	1.91 (±1.80)	7.49 (±1.91)	3.4 (±1.8)	1.35	62.0	42.3

1178

bioRxiv preprint doi: https://doi.org/10.1101/2021.11.13.468347; this version posted November 13, 2021. The copyright holder for this preprint (which was not certified by peer review) is the author/funder. All rights reserved. No reuse allowed without permission.

Table 3. Quantitative analysis of the k-fiber organization

Data set / Analysis	KMT density at the kinetochore [KMT/µm^2]	Neighborhood KMT-KMT distance at the kinetochore [nm]	Tortuosity of KMTs	Percentage of curved KMTs [%]	Area of k-fibers [µm^2]	Density of k-fibers [%]
Spindle #1	0.07 (± 0.05)	61 (± 11)	1.09 (± 0.10)	36.1	0.063 (± 0.085)	34 (± 27)
Spindle #2	0.09 (± 0.06)	65 (± 12)	1.06 (± 0.06)	21.4	0.068 (± 0.092)	70 (± 25)
Spindle #3	0.06 (± 0.04)	66 (± 12)	1.11 (± 0.11)	39.5	0.080 (± 0.150)	59 (± 39)

bioRxiv preprint doi: https://doi.org/10.1101/2021.11.13.468347; this version posted November 13, 2021. The copyright holder for this preprint (which was not certified by peer review) is the author/funder. All rights reserved. No reuse allowed without permission.

Table 4. Analysis of the potential association of KMT minus ends with other neighboring KMT lattices

Data set	Analysis	Association distance [nm]						
		25	**30**	**35**	**45**	**50**	**75**	**100**
Spindle #1	**No. of KMTs**	50	86	141	229	263	317	333
	Percentage of KMTs [%]	6.7	11.5	18.9	30.6	35.2	42.4	44.5
Spindle #2	**No. of KMTs**	32	67	108	181	213	290	299
	Percentage of KMTs [%]	3.0	6.3	10.1	16.9	19.9	27.1	27.9
Spindle #3	**No. of KMTs**	24	54	87	145	166	201	218
	Percentage of KMTs [%]	3.6	8.0	13.0	21.5	24.6	29.8	32.3

bioRxiv preprint doi: https://doi.org/10.1101/2021.11.13.468347; this version posted November 13, 2021. The copyright holder for this preprint (which was not certified by peer review) is the author/funder. All rights reserved. No reuse allowed without permission.

Table 5. Analysis of the potential association of KMT minus ends with other neighboring non-KMT lattices

Data set	Analysis	Association distance [nm]						
		25	**30**	**35**	**45**	**50**	**75**	**100**
Spindle #1	**No. of KMTs**	63	110	172	244	278	362	386
	Percentage KMT [%]	8.4	14.7	23.0	32.6	37.2	48.4	51.6
Spindle #2	**No. of KMTs**	272	343	401	533	578	703	739
	Percentage KMT [%]	25.5	32.0	37.4	49.7	53.9	65.6	68.9
Spindle #3	**No. of KMTs**	55	100	148	244	280	384	427
	Percentage KMT [%]	8.2	14.8	22.0	36.2	41.5	57.0	63.4

bioRxiv preprint doi: https://doi.org/10.1101/2021.11.13.468347; this version posted November 13, 2021. The copyright holder for this preprint (which was not certified by peer review) is the author/funder. All rights reserved. No reuse allowed without permission.

Table 6. Analysis of the potential association of KMT lattices with other neighboring KMT minus ends

Data set	Number of associations according to the given association distances [nm]						
	25	**30**	**35**	**45**	**50**	**75**	**100**
Spindle #1	54	102	184	342	412	733	1073
Spindle #2	41	88	146	298	379	703	946
Spindle #3	24	60	106	197	241	409	619

bioRxiv preprint doi: https://doi.org/10.1101/2021.11.13.468347; this version posted November 13, 2021. The copyright holder for this preprint (which was not certified by peer review) is the author/funder. All rights reserved. No reuse allowed without permission.

Table 7. Analysis of the potential association of KMT lattices with other neighboring non-KMT minus ends

Data set	Number of associations according to the given MT-MT distances [nm]						
	25	**30**	**35**	**45**	**50**	**75**	**100**
Spindle #1	141	265	438	771	932	1733	2530
Spindle #2	96	194	357	736	956	1961	2852
Spindle #3	88	213	352	636	798	1470	2205

bioRxiv preprint doi: https://doi.org/10.1101/2021.11.13.468347; this version posted November 13, 2021. The copyright holder for this preprint (which was not certified by peer review) is the author/funder. All rights reserved. No reuse allowed without permission.

Table 8. The average number of associations with MT lattices

Data set	MT type	Number of associations according to the given MT-MT distances [nm]				
		25	30	35	45	50
Spindle #1	KMTs	3.4 (± 2.0)	5.7 (± 3.1)	7.7 (± 4.1)	10.9 (± 5.5)	12.5 (± 6.3)
	non-KMTs	2.9 (± 2.1)	4.4 (± 3.4)	5.8 (± 4.5)	8.1 (± 6.2)	9.2 (± 7.0)
Spindle #2	KMTs	2.8 (± 1.8)	4.1 (± 2.7)	5.6 (± 3.5)	8.8 (± 5.2)	10.3 (± 6.0)
	non-KMTs	2.0 (± 1.3)	2.7 (± 1.9)	3.6 (± 2.7)	5.4 (± 4.1)	6.3 (± 4.7)
Spindle #3	KMTs	3.3 (± 2.0)	6.0 (± 3.3)	7.8 (± 4.2)	11.0 (± 5.6)	12.6 (± 5.3)
	non-KMTs	2.5 (± 1.9)	3.8 (± 3.2)	4.9 (± 4.1)	6.8 (± 5.6)	7.7 (± 6.3)
Average	KMTs	5.4 (± 3.1)	9.3 (± 5.0)	14.3 (± 6.1)	18.8 (± 9.8)	22.4 (±10.7)
	non-KMTs	4.4 (± 3.0)	7.5 (± 5.0)	10.1 (± 6.4)	15.7 (± 9.5)	18.2 (±10.9)

bioRxiv preprint doi: https://doi.org/10.1101/2021.11.13.468347; this version posted November 13, 2021. The copyright holder for this preprint (which was not certified by peer review) is the author/funder. All rights reserved. No reuse allowed without permission.

Table 9. The average length of associations with MT lattices

Data set	MT type	Length of associations according to the given MT-MT distances [nm]				
		25	30	35	45	50
Spindle #1	KMTs	103.2 (± 89.3)	148.5 (± 97.3)	197.1 (± 117.8)	265.3 (± 118.2)	291.3 (± 121.3)
	non-KMTs	65.9 (± 46.7)	92.4 (± 64.2)	120.8 (± 80.4)	169.0 (± 105.7)	188.0 (± 111.71)
Spindle #2	KMTs	94.2 (± 86.8)	124.0 (± 88.2)	164.6 (± 104.6)	262.5 (± 137.1)	310.1 (± 154.0)
	non-KMTs	66.6 (± 57.9)	85.5 (± 71.9)	107.0 (± 85.3)	159.7 (± 121.4)	183.0 (± 135.0)
Spindle #3	KMTs	94.2 (± 86.8)	124.0 (± 88.2)	164.6 (± 104.6)	262.5 (± 137.1)	310.1 (± 154.0)
	non-KMTs	84.5 (±69.8)	137.5 (± 101.7)	195.1 (± 124.0)	274.6 (± 135.7)	299.8 (± 137.3)
Average	KMTs	83.9 (± 56.4)	118.5 (± 63.8)	162.5 (± 70.1)	234.2 (± 97.9)	260.8 (±101.7)
	non-KMTs	67.7 (±44.5)	96.1 (±59.2)	128.0 (± 74.6)	186.3 (±93.1)	211.1 (±102.7)

bioRxiv preprint doi: https://doi.org/10.1101/2021.11.13.468347; this version posted November 13, 2021. The copyright holder for this preprint (which was not certified by peer review) is the author/funder. All rights reserved. No reuse allowed without permission.

Table 10. Tomographic data sets as used throughout this study

Metadata / Data set	Original data set	Montages (X/Y)	Number of serial sections [300 nm each]	Estimated tomographic volume [µm^3]	Data size [Gb]
Spindle #1	T_0475	2x3	22	598	46.5
Spindle #2	T_0479	2x3	29	996	77.9
Spindle #3	T_0494	2x3	35	904	71.9

bioRxiv preprint doi: https://doi.org/10.1101/2021.11.13.468347; this version posted November 13, 2021. The copyright holder for this preprint (which was not certified by peer review) is the author/funder. All rights reserved. No reuse allowed without permission.

Key resources table

Reagent type (species) or resource	Designation	Source or reference	Identifiers	Additional information
Strain, strain background (HeLa, Kyoto)	Gerlich Lab	IMBA, Vienna, Austria	-	-
Software, algorithm	SerialEM Boulder Laboratory for 3-Dimensional Electron Microscopy of cells Colorado	https://bio3d.colorado.edu/SerialEM/	-	-
Software, algorithm	IMOD Boulder Laboratory for 3-Dimensional Electron Microscopy of cells Colorado	http://bio3d.colorado.edu/imod	-	-
Software, algorithm	Amira Thermo Fisher Scientific	AmiraZibEdition	-	-
Software, algorithm	ASGA Robert Kiewisz / Müller - Reichert Lab Dresden	https://github.com/RRobert92/ASGA	-	https://kiewisz.shinyapps.io/ASGA
Software, algorithm	ASGA - 3D Viewer Robert Kiewisz / Müller - Reichert Lab Dresden	https://github.com/RRobert92/ASGA_3DViewer	-	https://cfci.shinyapps.io/ASGA_3DViewer/